Quantification of native mRNA dynamics in living neurons using fluorescence correlation spectroscopy and reduction-triggered fluorescent probes

Hirotaka Fujita (藤田 裕貴)[1], Ryota Oikawa (及川 涼太)[2], Mayu Hayakawa (早川 真由)[2], Fumiaki Tomoike (友池 史明)[2], Yasuaki Kimura (木村 康明)[2], Hiroyuki Okuno (奥野 浩行)[3], Yoshiki Hatashita (畑下 慶紀)[1], Carolina Fiallos Oliveros[1], Haruhiko Bito (尾藤 晴彦)[4], Toshio Ohshima (大島 登志男)[1], Satoshi Tsuneda (常田 聡)[1], Hiroshi Abe (阿部 洋)[2], and Takafumi Inoue (井上 貴文)[1*]

[1]Department of Life Science and Medical Bioscience, School of Advanced Science and Engineering, Waseda University, Tokyo, Japan; [2]Department of Chemistry, Graduate School of Science, Nagoya University, Aichi, Japan, [3]Graduate School of Medical and Dental Sciences, Kagoshima University, Kagoshima, Japan, [4]Department of Neurochemistry, Graduate School of Medicine, The University of Tokyo, Tokyo, Japan

Running title: Quantification of mRNA dynamics by FCS and RETF probe

[*]To whom correspondence should be addressed: Takafumi Inoue: Laboratory of Neurophysiology, Department of Life Science and Medical Bioscience, Faculty of Science and Engineering, Waseda University, 2-2 Wakamatsu-cho, Shinjuku-ku, Tokyo 162-8480, Japan; Tel.: +81-3-5369-7328; e-mail: inoue.t@waseda.jp

Keywords: fluorescence correlation spectroscopy (FCS), mRNA, neuron, RNA transport, live-cell imaging, reduction-triggered fluorescence (RETF), transcription, gene regulation, hippocampus, cellular dynamics

ABSTRACT

RNA localization in subcellular compartments is essential for spatial and temporal regulation of protein expression in neurons. Several techniques have been developed to visualize mRNAs inside cells, but the study of the behavior of endogenous and nonengineered mRNAs in living neurons has just started. In this study, we combined reduction-triggered fluorescent (RETF) probes and fluorescence correlation spectroscopy (FCS) to investigate the diffusion properties of activity-regulated cytoskeleton-associated protein (*Arc*) and IP3 receptor isoform 1 (*Ip3r1*) mRNAs. This approach enabled us to discriminate between RNA-bound and unbound fluorescent probes and to quantify mRNA diffusion parameters and concentrations in living rat primary hippocampal neurons. Specifically, we detected the induction of *Arc* mRNA production after neuronal activation in real time. Results from computer simulations with mRNA diffusion coefficients obtained in these

analyses supported the idea that free diffusion is incapable of transporting mRNA of sizes close to those of *Arc* or *Ip3r1* to distal dendrites. In conclusion, the combined RETF–FCS approach reported here enables analyses of the dynamics of endogenous, unmodified mRNAs in living neurons, affording a glimpse into the intracellular dynamics of RNA in live cells.

Introduction

The transport and local translation of mRNA play crucial roles in synaptic functions in neurons (1–3). A variety of mRNAs are delivered to dendrites and axons and translated in response to synaptic activation (4). To date, genetic and biochemical approaches have been used to visualize mRNAs in living cells. Aptamer-based RNA imaging techniques have been widely applied (5). The MS2 system is the most popular one, which enables highly sensitive and specific imaging of transcripts (6). However, this method requires genetic manipulation of the target RNA sequence by inserting multiple aptamer-binding sequences. Many studies using the MS2 system exogenously expressed abundant target RNAs containing the MS2-binding sequence, which can lead to biased results due to overexpression. Singer's group knocked in the MS2 or PP7-binding sequence to the 3'-untranslated regions (UTRs) of target RNAs (7, 8), which avoids the exogenous overexpression effects, but requires tedious efforts to produce knock-in animals.

Switch-on fluorogenic hybridization probes have been used to investigate the dynamics of unmodified mRNAs. The peptidic Pumilio homology domain (PUM-HD) RNA probe binds to RNA in a sequence-specific manner by recognizing eight conterminous bases, thus allowing spatiotemporal analysis of endogenous RNA localization (9, 10). It requires optimization of the amino acid sequence for each target. Fluorescent oligonucleotide hybridization probes such as molecular beacons (11, 12), in which internally quenched fluorescent antisense probes are used, and RNA-targeting Cas9 (13) enable the mapping of RNA localization with high versatility. Because of the weak signal and background fluorescence derived from unbound probes, the range of target mRNA species is limited. Turner-Bridger et al. have succeeded in labeling native RNA in distal axons of neurons using molecular beacon probes with highly inclined and laminated optical sheet (HILO) microscopy; however, it was difficult to detect mRNA signals in the soma and proximal axon owing to nonspecific signals derived from probes detached from mRNAs (14).

To label native mRNA, we used the reduction-triggered fluorescence (RETF) probe technique (15), which consists of a pair of oligonucleotides conjugated with a nonfluorescent azidomethyl fluorescein derivative as a fluorogenic tag and with triphenylphosphine as a reducing reagent (Fig. 1A). The RETF probe emits fluorescence after the pair of probes hybridize to the target mRNA side by side and a reducing reaction between them occurs. The RETF probe detected endogenous mRNA at the single-nucleotide-mismatched level in fixed bacterial and living human cells (15, 16), and distinguished between prelariat and lariat RNA structures in the intron (17). Although the high signal-to-background ratio (S/B) of the RETF probe, reaching 2400:1 (15), stands out among RNA probes [e.g. the best S/B of FRET-based RNA probes reported was 50:1 (18)], background fluorescence derived from reduced probes dissociated from target mRNA complicates quantitative analyses.

We adopted the fluorescence correlation spectroscopy (FCS) method to overcome the

background issue of the RETF probe. FCS allows quantification of diffusion coefficient and concentration of fluorescently labeled biomolecules in living cells based on fluorescence fluctuation analysis within a tiny focal spot, which is small enough to measure molecular dynamics in not only neuronal dendrites (19), but also spines (20). Autocorrelation functions calculated from the fluorescence fluctuation are fitted with theoretical diffusion models, and quantitative parameters are deduced. With fluorescence fluctuation spectroscopy (FFS), which is closely related to FCS, quantitative measurements of MS2-labeled *β-actin* mRNA were performed (21) and protein–mRNA interactions were revealed (22). FCS discriminates diffusing molecule species of different diffusion coefficients, which are mainly influenced by the radius of gyration of the diffusion molecules and the viscosity of the medium. The radii of gyration of mRNA bound with RETF probes and free RETF probes were expected to be sufficiently different to be distinguished by diffusion coefficients.

Numerous mRNA types, such as activity-regulated cytoskeleton protein (*Arc*; also known as *Arg3.1*), inositol 1,4,5-trisphosphate receptor type 1 (*Ip3r1*), and Ca^{2+}/CaM kinase IIα (*CaMKIIα*), are distributed in the dendrites of central nervous system neurons. The immediate early gene, *Arc*, plays a role in activity-dependent synaptic modifications. *Arc* mRNA is robustly expressed by synaptic activity, and then rapidly delivered throughout dendrites (23, 24). After stimulation, *Arc* mRNA appeared in the cytoplasm within 15 min, and translocated to the tips of distal dendrites within 1 h (25, 26). Newly synthesized *Arc* mRNA transcripts are selectively localized at activated synapses by an activity-dependent mRNA degradation mechanism, which eliminates *Arc* mRNA from inactive dendritic regions (27). The localization and translation of *Arc* mRNA are associated with endocytosis of α-amino-3-hydroxy-5-methyl-4-isoxazolepropionic acid (AMPA)-type glutamate receptors, thus contributing to the regulation of synaptic efficacy (28, 29). In addition to synaptic modification, Arc protein forms a retrovirus-like capsid structure and transfers mRNA between neurons (30, 31). A previous study using the MS2 system reported that exogenously expressed RNA containing the 3'-UTR of *Arc* mRNA moved bidirectionally at a velocity of 6 to 65 μm/min in dendrites (32). Furthermore, the RNA localized at or near the base of dendritic spines with a high probability (33). A knock-in mouse line where *Arc* mRNA was labeled with an aptamer-binding cassette allowed visualization of the endogenous activity-induced transcription of individual mRNAs (8).

Ip3r1 is an intracellular Ca^{2+} release channel expressed in central nervous system neurons including cerebellar Purkinje cells and hippocampal neurons (34). It plays pivotal roles in synaptic plasticity in the hippocampus and cerebellum (35–37). While the MS2 system was previously used to visualize the 3'-UTR of *Ip3r1* mRNA, its use was limited to the detection of colocalization with RNA-interacting proteins (38, 39). Thus, the dynamics of *Ip3r1* mRNA is poorly understood.

In this study, we aimed to develop a technique to assess the dynamics of nonengineered endogenous mRNAs using the RETF probe together with FCS. We first tested whether RETF probes can detect *Arc* and *Ip3r1* mRNAs in neuron. Subsequently, we employed FCS to discriminate mRNA-unbound and -bound probes by the difference in their diffusion coefficients. And finally, we tried out this approach by monitoring changes in the diffusion coefficient and concentration

of *Arc* mRNA by neuronal activation. This combined RETF probe–FCS method, as demonstrated here, has a potential to distinguish RNA-bound and -unbound probes by diffusion patterns, providing semi-quantitative estimations of endogenous and unmodified mRNAs in living neurons.

RESULTS

Fluorescence derived from RETF probes increases after introduction by patch clamp

We designed two RETF probes targeting different mRNA locations, termed target 1 and target 2, for *Arc* mRNA and *Ip3r1* mRNA, respectively. The target sequences were chosen from locations where successful *in situ* hybridization results were reported. To test whether the RETF probes can detect target RNAs in living neurons, we introduced sets of RETF probes targeting *Arc* mRNA or *Ip3r1* mRNA into hippocampal neurons by the whole-cell patch clamp method. The RETF probe-derived fluorescence signal started to increase after patch clamp formation in both soma and dendrites, and was saturated within 40 min, while a mismatched probe pair consisting of the azidomethyl fluorescein (Az) probe of target 1 and the triphenylphosphine (TPP) probe of target 2 *Arc* RETF probes yielded no fluorescence signal more than autofluorescence (Fig. 1B–C). Fluorescence signals derived from RETF probes targeting *Arc* or *Ip3r1* mRNAs spread across the cytosol (Fig. 1D).

FCS measurement with RETF probe

Although the increase in fluorescence derived from the RETF probes was clear, there was a possibility that not all of the fluorescence signal was emitted from RETF probes bound to target mRNAs, as some of it may have been from RETF probes detached from target mRNAs. To test this, we performed FCS, which was expected to distinguish between the RNA-bound and unbound forms of RETF probes by virtue of diffusion coefficients. As a control probe, we used a fluorescein-conjugated scramble probe: a 15-base single-stranded DNA of a random sequence conjugated with fluorescein instead of reduced Az. The sequence was confirmed not to have a match in the rat RNA database.

Calibration of the FCS system

Laser power adjustment and focal volume calibration should be done periodically (Fig. 2A). The irradiance of the 488-nm blue laser was adjusted to around 5 μW at the tip of the 60× objective, which was determined not to saturate the absorption of the fluorophore within the focused laser spot (40). The focal volume was determined as horizontal and vertical radii (r_{xy} and r_z, respectively) by fitting an autocorrelation function of 10 nM Rhodamine 6G in PBS buffer to a one-component 3D diffusion model, with a fixed diffusion coefficient of 414 $\mu m^2/s$ (41). Diameter of the detection pinhole built in the FV-300 confocal system, which also determines the effective focal volume for FCS, was fixed to 150 μm for all FCS experiments, which was larger than the one optimal for confocality for the objective (100 μm) due to the low signal condition in this study. The resultant r_{xy} and r_z were 0.34 and 3.26 μm, respectively. The structure parameter ($\gamma = r_z/r_{xy}$; 9.6) was larger than the benchmark values (ranging 3–8) in optimally aligned systems, and γ was 5.6 with the 100-μm-diameter pinhole in our system.

FCS measurement with RETF probes in in vitro

In an *in vitro* condition, a RETF probe for *Arc* yielded autocorrelation functions after mixed with *in vitro*-transcribed *Arc* RNA (Fig.

S1B), which were fitted well to a two-component diffusion model irrespective of addition of the scramble probe. Addition of RNaseA to the mixtures eliminated the slower diffusion components, leaving the faster diffusion component unchanged (Fig. S1C). The slower diffusing component was thought to represent the RNA-RETF probe complex, because it was diminished by the RNase addition and the concentration of it (C_{slow}) was decreased by the dilution with the scramble probe solutions (Fig. S1Dd). And we consider that the faster diffusion component observed in the RNA-RETF probe mixture without addition of the scramble probe represented RETF probe molecules detached from RNA, because its diffusion coefficient (D_{fast}) was very similar to the scramble probe (Fig. S1Da). The concentration range of the fast and slow components (2–30 nM) indicates that our FCS system faithfully measures concentration at the low nanomolar range in cell-free condition. Contribution of RETF probes that were directly reduced by the triphenylphosphine-tagged probes without binding to RNA should be negligible, because the fluorescence signal was not detectable in an *in vitro* RETF experiment with RETF probes without RNA.

FCS measurement with RETF probe in neurons

In intracellular experiments, neurons were loaded with the target 1 and/or target 2 RETF probes, or with the scramble probe together with Alexa 594 biocytin by whole-cell patch clamp (Fig. 2Ba) in a separate inverted microscope setup from the confocal/FCS microscope in this study. If the confocal/FCS microscope allows the patch-clamp experiment, the same microscope can be used. Substances may be alternatively loaded by micro injection, while it is much more difficult to apply to neurons than to cell lines because neurons are fragile. The success rate of the patch-clamp dye loading method was 80% (147 trials) in this study. If substance loading by patch-clamp and FCS measurement are performed on a single microscope setup, keeping patch-clamping during FCS measurements is possible, however that is not suggested because continuous exchange of contents between pipette and cytosol makes conditions complex.

The co-injected marker, Alexa 594 biocytin dye, was necessary to identify the target cell after changing microscope and to capture clear shapes of the cells, because the fluorescence intensity of RETF probes is too dim to identify easily and to capture confocal images of sufficient quality. Due to the high sensitivity of FCS, a scant crosstalk from the marker fluorescence channel to the FCS fluorescence channel would cause serious deformations of autocorrelation curves. There was no detectable contamination of the Alexa 594 fluorescence to the FCS recording channel.

A stainless chamber holding a cover slip with neurons was transferred from the microscope for patch-clamp to the confocal/FCS microscope, and FCS measurement was performed. Neurons injected with probes and the marker Alexa 594 biocytin were identified by epi-fluorescence microscopy with the Alexa 594 biocytin fluorescence and confocal images were taken and stored (Fig. 2Bb). FCS recording was performed at earliest 5 min after the patch-clamp loading to gain enough RETF signals (see Fig. 1C).

The recording point for FCS was located at the cytosol in the soma or locations in dendrites 30–50 μm away from the soma. The fluorescence intensity recorded at single points in cells often rapidly decayed during the first 2–3 s and then became relatively stable. We considered that this rapid decay of fluorescence signal derived from immobile

fluorescence sources, which was not the subject of this study. Hence, at each recording point, we omitted the first 5 s irradiance (Fig. 2Bc) and then started a series of FCS recordings (Fig. 2Bd; 5–12 times for 20 s in each cell).

Waiting time for obtaining meaningful FCS results after loading RETF probe may depend on factors such as the concentration of target mRNA and the location of recording point in the cell, e.g. cell body and distal or proximal dendrite. If an autocorrelation function is not smooth enough for fitting with diffusion models even after repeated records are averaged, fluorescence signal is too weak for FCS analysis and more time should be waited (~30 min; see the saturation of fluorescence signals in Fig. 1C). If acceptable signal intensity is not gained after trying several cells, it is possible that the target mRNA concentration in the target cell is not high enough for the RETF-FCS method or that the choice of target sequence is not appropriate. Although in cell-free FCS, longer recording time compensates for weak fluorescence signals, longer recording time, or more repetitions, results in too much photobleaching in intracellular FCS. Thus the minimum limit of target RNA concentration is higher in intracellular FCS than cell-free FCS. More photo-stable fluorescence tags are awaited for better sensitivity of intracellular FCS.

Dendritic shape and diffusion models

Knowing the dendrite size is necessary for choice of appropriate diffusion models (42). The dendritic width of target neurons for FCS measurement was measured at 30–50 µm away from the soma on Alexa 594 biocytin images (Fig. 2Ca; see Experimental Procedures), where FCS measurements in the dendrite were performed. Accordingly, the dendrite diameter ranged from 1.9 to 3.0 µm (2.5 ± 0.3 µm; Fig. 3B). The confinement degree is expressed as d/r_i using the dendritic diameter d and the focal radius r (42). Diffusion in the z-direction, perpendicular to the coverslip surface, is negligible because the d/r_z value (0.75) was smaller than 0.833 (42). In the axial direction of the dendrite, the diffusion space was confined by the dendritic boundaries since the average d/r_{xy} value was 7.2. Thus, we adopted a confined diffusion model to the autocorrelation functions recorded in dendrites with $d_z = 2.5$ µm and the confinement parameter $Y = 7.2$ (19). In the case of somata, a standard three-dimensional (3D) diffusion model was used to fit to autocorrelation functions (19).

Photobleaching

Photobleaching of fluorescence molecules in cytosol during single FCS recording led to an artefact, which gave rise to a very slow artifactual diffusion fraction (43). Thus, photobleaching was assessed by fitting each fluorescence trace to a double exponential equation: $i(t) = i_0 + i_1 \cdot \exp(t/t_{B1}) + i_2 \cdot \exp(t/t_{B2})$, and deducing a photobleaching parameter i_{20}/i_0, which represents fluorescence decay during the 20 s measurement period (Fig. S2). The photobleaching magnitude differed among the probe sets and, in particular, those with the scramble probe and the combination of targets 1 and 2 of *Arc* and *Ip3r1* probes were larger than those of singly loaded probes (Fig. S2A). There was a positive correlation between the photobleaching magnitude and the probe concentration (Fig. S2B), which is consistent with a previous study in which the photobleaching effect was smaller in weakly fluorescent cells (43). To minimize the photobleaching effect, we applied a photobleaching correction before the calculation of autocorrelation functions (Fig. 2Cb; see Experimental Procedures).

Autocorrelation function and fitting with diffusion models

Autocorrelation functions calculated from each series of 20 s fluorescence recordings were averaged for each cell and fitted with one- and two-component diffusion models (Figs. 2Cc and 4B–C). As the residual of the fitting of both RETF and scramble probes showed that the one-component model did not yield acceptable fitting, the two-component diffusion models were used in the rest of this study. Fitting to a two-component model is common in intracellular FCS studies because of the existence of slow diffusion fractions (19, 43, 44), which are thought to derive from autofluorescence, nonspecific binding of fluorescent probes to intracellular molecules that slowly diffuse, and other unknown factors affecting the shape of autocorrelation function. In this study, the contribution of autofluorescence seems small, because no reasonable autocorrelation curves were obtained in neurons without loading fluorescent probes (data not shown).

The diffusion parameters were deduced by fitting averaged autocorrelation functions in each cell to the two-component model with triplet-state correction (Fig. 5). The faster and slower diffusing components of the scramble probe, therefore, represent freely diffusing ones and non-specific binding of it to slowly diffusing molecules together with other unknown factors, respectively. The several-fold-smaller D_{fast} of the scramble probe in neurons (ranging 62–68 $\mu m^2/s$ in soma and dendrite) compared with its D value in cell-free medium ($1.3\times10^2 \pm 5.0$ $\mu m^2/s$, n = 4 in water, Fig. S1) was consistent with previous intracellular FCS studies (19, 43–45) showing much smaller D values in intracellular FCS recordings than those obtained in the cell-free FCS.

In the case of the RETF probes, the averaged autocorrelation functions of each cell show fluctuation at the shortest lag ranges (< 0.01 ms). This fluctuation was presumably caused by low occurrence of correlated events, i.e. the concentration of fluorophore was low. This notion is supported by the result that the fluctuation at the same lag range of the scramble probe, of which fluorescence intensity, and thus concentration, was higher than those of RETF probes, was smaller than those of the RETF probes (Fig. 4A). The small event number may have manifested the stochastic nature of the triplet-state transition. To reduce this fluctuation of autocorrelation functions of the RETF probes, more repeat of recording was necessary, but photo-bleaching prevented it. This fluctuation at the shortest lags may be inevitable with the low concentration of endogenous mRNA. The impact of the fluctuation to the fitting result was investigated by swapping the shorter lag part of an autocorrelation function of a cell with those of other cells (Fig. S3). Fitting of the chimeric autocorrelation functions to the two-component 3D diffusion model resulted in varying D_{fast} and diffusion coefficient of the slower component (D_{slow}), relatively steady concentration of faster component (C_{fast}), and very steady C_{slow} values (Fig. S3C). Thus the accuracy of the diffusion coefficients is impaired by the fluctuation of the shorter lag range of autocorrelation function for each cell, which requires enough cell number for reliable results, while the concentration values are not affected much.

Although the slower part of the autocorrelation functions (≥ 0.01 ms) of the RETF probes look fitted well to the two-component diffusion models (Fig. 4B–C), diffusing molecule species may consist of not only the free RETF probes and RETF probes bound with full-length target mRNAs but also RETF probes bound with different sized degraded target RNAs in addition to the non-

specific binding to intracellular molecules and other factors. Thus the two-compartment diffusion models may reflect complex convolutions of such complicated diffusing molecular species, which is a shortcoming of FCS that it cannot handle many diffusion species precisely, but the FCS results should still reflect features of the binding of RETF probes to target RNA.

The range of D_{fast} of the RETF probes in neurons (24–73 $\mu m^2/s$, range of medians of cells of the same probe set) was close to that of the scramble probe (61–66 $\mu m^2/s$), implying that the faster component of the RETF probes in cells mainly reflect free RETF probes. The D_{fast} values of the RETF probes in cells, especially in the soma, varied more widely than those of the scramble probe, and the unevenness differed among the RETF probe types (Fig. 5A), suggesting that the faster component of the RETF probes may consist of not only free RETF probes but also RETF probes bound to fragmented mRNAs. Free RETF probes may have derived from those once bound to the target RNA then detached as was seen in the cell free experiment (Fig. S1), while RETF probes that underwent a reduction reaction with reducing probes in the cytosol or in the patch pipette without binding target RNAs were negligible because, in a control experiment, *Arc* RETF probes introduced into HEK cells, which do not express *Arc* mRNA (31), did not show detectable fluorescence or reasonable autocorrelation curves (data not shown).

C_{fast} and C_{slow} of the scramble probe had a positive correlation in both soma and dendrite (Fig. S4A), indicating that the slower diffusing component of the scramble probe contains not only the background of unknown causes inherent in the intracellular FCS analysis (19, 43, 44), which rides on slow diffusing ranges of the autocorrelation curve, but also non-specifically bound scramble probes with slowly diffusing molecules. In the case of RETF probes, such non-specific binding should be much smaller because the overwhelming non-fluorescent RETF probes mask most of the non-specific binding sites. Thus, C_{slow} of RETF probes may represent binding to the target mRNAs in addition to the background inherent in the intracellular FCS analysis and non-specific binding that is presumably much smaller than that of the scramble probe. This idea that the slower diffusing component of the RETF probes reflected their binding to mRNAs is further supported by the following arguments: firstly, the ratio of C_{slow} to the total concentration (C_{slow}/C_{total}, where $C_{total} = C_{fast} + C_{slow}$) of single *Arc* probes and of single and both *IP3R* probes together were much larger than that of the scramble probe and of both *Arc* probes together (Fig. 5C). Secondly, the brightness of particles in the slower diffusing component relative to the faster diffusing component ($\varepsilon_{slow}/\varepsilon_{fast}$) was larger in cells loaded with targets 1 and 2 together than in those loaded with single RETF probes (Fig. 5Bc). This is because mRNA molecules bound to two RETF probes should be double as bright as those bound to single RETF probes (Fig. 5D). However, the actual value of $\varepsilon_{slow}/\varepsilon_{fast}$ was not 2 but around 1.2–1.4 because not all target RNAs are bound by the two types of RETF probes: some target RNAs may have degraded and lost one of the RETF probe binding sites, and some of the bound RETF probes may have been photobleached. Altogether, we consider that the slower component of the RETF probes contains an evaluable RNA-bound RETF probe fraction, however it was not separable from non-specific binding of RETF probes with slowly diffusing molecules as seen with the scramble probe, which made quantitative evaluation of RNA-bound RETF probes difficult.

To evaluate the confined diffusion model

applied to the dendrite, the autocorrelation curves obtained in the dendrite were also fitted with the 3D diffusion model (Fig. 5). As a result, the overall tendency did not differ, and the diffusion parameters, especially in D_{slow} and $\varepsilon_{slow}/\varepsilon_{fast}$, with the 3D diffusion model in the dendrite were closer to those in the soma than those with the confined diffusion model in the dendrite.

Arc mRNA increases upon TTX withdrawal

Although the slow diffusing component of RETF probes in neuron possibly contains the mRNA-bound RETF probes, other slow components as seen with the control scramble probe are mingled with it and make interpretation of the mRNA-bound RETF probe diffusion difficult. To further characterize the mRNA-bound RETF probe fraction, we examined changes in the FCS properties during *Arc* transcription induction by neuronal activation. Neuronal activity was suppressed by incubation with 2 μM tetrodotoxin (TTX) for 2 days, and then TTX was washed out, which induces rapid and robust *Arc* transcription (8, 46, 47). A reverse transcription polymerase chain reaction (RT-PCR) assay showed that the *Arc* mRNA levels increased within 20 min, and reached fourfold within 40 min after TTX removal (Fig. 6A).

Neurons incubated with TTX were loaded with an *Arc* RETF probe (target 2) or the scramble probe by the whole-cell patch clamp method, and FCS was performed under HEPES-buffered saline (HBS) with 2 μM TTX. Then, the medium was washed with TTX-free HBS. Thereafter, FCS measurements were performed at the same locations in each cell every 20 min for 1 h. Two concentrations of the RETF probe, 2 and 10 μM, were used to test the saturation level of the probe. In control experiments using the *Arc* RETF probe without TTX removal and the scramble probe with TTX removal, the C_{slow} values were decreased rather than increased during the time course, which was interpreted as photobleaching of probes during the series of measurements. TTX withdrawal led to overall increases in C_{slow} with the RETF probe in both soma and dendrites (Fig. 6Ba). In the soma, C_{slow} slightly decreased 20 min after TTX withdrawal, possibly because of photobleaching during the series of measurements, and then it increased after 40 min ($p < 0.05$, paired *t*-test between 20 and 40 min). The initial C_{slow} values of the scramble probe were larger or about the same level as C_{slow} of the *Arc* RETF probe 40–60 min after TTX removal in soma and dendrite, respectively. It does not mean that C_{slow} of the *Arc* RETF probe was below the background level: non-specific binding is a major fraction of C_{slow} of the scramble probe, while the non-specific binding of fluorescent RETF probes should be very small because the overwhelming non-fluorescent RETF probes should mask the non-specific binding sites. Therefore, C_{slow} of RETF probes is smaller than that of the scramble probe. $\varepsilon_{slow}/\varepsilon_{fast}$ of the RETF probes was increased by the TTX removal, while it decreased in the control experiments (Fig. 6Bb). Although the increment of $\varepsilon_{slow}/\varepsilon_{fast}$ was not large, there is a possibility that a small portion of RETF probe–target RNA complexes formed aggregates or incorporated in ribonucleoprotein particles (RNPs) (7, 48). These results strongly suggest that the increase in C_{slow} of the RETF probe reflected activation of *Arc* mRNA production by neuronal activation.

Because the absolute C_{fast} values differed among the conditions owing to the difference in RETF probe concentration, and the difference in the fluorescence emission nature of the RETF and scramble probes (Fig. 7A), normalized C_{fast} time courses were plotted (Fig.

7B). In the control experiments, that is, the RETF probe without TTX withdrawal or the scramble probe, C_{fast} decreased, possibly because of photobleaching during the series of measurements. In the RETF probe with TTX withdrawal experiment, C_{fast} increased in the dendrites, but not in the soma (Fig. 7B). While D_{fast} of the RETF probe fluctuated, it was larger than the intracellular diffusion coefficient of mGFP [D = 13.8 ± 0.9 μm^2/s, mean ± s.e.m. (45)] throughout the measurement (Fig. 7C).

Simulation of RNA distribution

With the median diffusion coefficient of *Arc* mRNA (D_{slow} = 2.1 μm^2/s) obtained in this study, the time course of the distribution pattern of newly synthesized *Arc* mRNA by free diffusion along the dendrite was simulated using a one-dimensional (1D) diffusion model along a tapering cylindrical shape (Fig. 8A). The simulated translocation of diffusing RNA reached 100 μm from the soma within 60 min, but it did not effectively reach 300 μm even after 120 min under conditions with an *Arc* mRNA half-life of 47 min (46) (Fig. 8B). Because RNA protection from degradation has been proposed as a factor explaining for an uneven mRNA distribution within the cell (49, 50), a scenario without the RNA degradation term was also tested. We found that diffusing RNA still did not reach 300 μm within 60 min (Fig. 8C). These simulation results indicate that the free diffusion of mRNAs is not sufficient for the distribution of mRNAs in distal dendrites within a reasonable time, and thus active transport mechanisms are necessary, as has been argued in previous reports (25, 26).

DISCUSSION

In this study, the dynamics and concentration of endogenous *Arc* and *Ip3r1* mRNA in living neurons were investigated, using the RETF probe technique and the FCS method. The RETF probe has a high S/B ratio due to its very low leaky fluorescence before target binding, which makes it a unique RNA labeling method among other methods such as molecular beacons (11, 12) and RNA-targeting dCas9 (13). The fact that reduced and fluorescent RETF probes remain fluorescent after detachment from the target RNA molecule is a shortcoming of this probe. The FCS method was able to constrain this issue by sorting the free detached RETF probes from mRNA-bound probes based on the different diffusion coefficients. However, as was seen with the scramble probe (Fig. 4C–D, scramble), autocorrelation function of intracellular FCS inherently accompanies slowly diffusing components (19, 43, 44), which overlap with the slow diffusing component deriving from RETF probe-RNA complex and make it difficult to isolate pure diffusion parameters of RNA-bound RETF probes. Also, the possibility of existence of different sized degraded target RNAs makes the interpretation of the fitting results difficult. However, the increase in the slow component of the RETF probe after *Arc* mRNA induction by TTX removal indicated that the slower diffusion component of the RETF probes still reflects increase in the RNA-bound RETF probes; hence, detection of changes in the *Arc* mRNA amount in single cells was achieved by the combination of RETF probe and FCS.

The total RNA concentration ([RNA$_{total}$]) is calculated as

$$[RNA_{total}] = [RNA_{bound}] \cdot \frac{[RETF_{total}] - [RNA_{bound}] + K_D}{[RETF_{total}] - [RNA_{bound}]}$$

(see Experimental Procedure). Because the C_{fast} value of the scramble probe (61 (56−66) and 38 (28−78) nM in soma and dendrites, respectively) was about one-tenth of the probe concentration in the patch pipette (0.5 μM), [RETF$_{total}$] is assumed to be 1000 nM, when we take the experiments in which patch pipette

was filled with 10 μM RETF into consideration here. K_D is assumed to range from 0.01 to 200 nM, according to a study in which K_D of RNA–DNA complex was measured using ß-actin RNA and a series of 17-mer antisense DNAs targeting several locations in the RNA (51). [RNA_{bound}] is less than the C_{slow} value (e.g., 7.1 nM at time 0) because C_{slow} consists of [RNA_{bound}] and presumably the concentration of RETF probes nonspecifically binding to intracellular molecules. Because [$RETF_{total}$] is much higher than [RNA_{bound}] and K_D, [RNA_{total}] can be approximated by the [RNA_{bound}] value with an error of at most 20%. The increase in C_{slow} of the Arc RETF probe (10 μM in pipette) was 3.0 (1.7−3.1) and 4.9 (3.6−4.9) nM 60 min after the TTX withdrawal in soma and dendrite, respectively (Fig. 6), representing an actual increase in RNA concentration with permissible errors.

The faster diffusing component of the RETF probes is considered to reflect the unbound reduced RETF probes deriving from RNA degradation of the RNA–RETF probe complex or from dissociation of the RETF probe from the RNA. Although dissociation rate constant of DNA-RNA complex is unknown, if we assume that the dissociation rate constant between RETF probe and the RNA target is not very different from that between RETF probe and DNA (10^{-2} order s^{-1}) (16), not ignorable portion of RNA-bound RETF may detach from RNA constantly, as was observed in the *in vitro* experiment (Fig. S1). The contribution of self-reduction of the RETF probe pair was negligible at the concentration ranges used in this study (15). The apparently large increase in C_{fast} of the RETF probe upon TTX removal in dendrites may reflect activity-dependent *Arc* mRNA production and degradation (27), at least in the dendrite.

Reported diffusion coefficients of transcripts vary widely, possibly because of differences in the labeling and measurement methods; the diffusion coefficients of *β-actin* mRNA were 3.8×10^{-3} $\mu m^2/s$ in neurons, 0.09 $\mu m^2/s$ in mouse embryonic fibroblasts (MEFs) (7), 0.1 $\mu m^2/s$ in the Cos7 cell line (52), and 5.3×10^{-3} $\mu m^2/s$ in A549 lung carcinoma cells (53), using the single-particle tracking method. Moreover, the diffusion coefficient of *β-actin/MS2* mRNA measured by FCS in MEFs was 0.35 $\mu m^2/s$ (21). Because the D_{slow} values in the present study were higher than those in these previous reports, especially for the *Arc* RETF probes in the dendrite (Fig. 5B), the slower diffusing component may include RETF probes bound to degraded RNAs, of which the diffusion coefficients were larger than those of probes bound to native RNAs.

In both soma and dendrite, C_{slow}/C_{total} of the double probe cases, where both the target 1 and 2 RETF probes were loaded, was smaller than those of the single probe cases for *Arc*, while it was not for *IP3R1* (Fig. 5C). This difference between the double probe and the single probes seen for *Arc* can be explained by both detachment of RETF probes from target RNA and fragmentation of RNA: a single RNA molecule bound with both target 1 and 2 RETF probes yields two separate fluorescent particles when one of the probes detaches or when the RNA is broken into small pieces and the two bound probes are separated. In the former case, C_{total} increases but C_{slow} does not. In the latter case, C_{total} increases as well, but C_{slow} does not increase as much as C_{total} does, because RETF probes bound with small RNA fragments may not contribute to increase in C_{slow} but in C_{fast}. Thus, the apparent smaller C_{slow}/C_{total} with the double probe than those with the single probes observed only for *Arc* may reflect that the degradation rate of *Arc* mRNA is greater than that of *IP3R1* mRNA, which is in good accordance with a report that *Arc* mRNA has an especially short half-life

(44) (Fig. 9), together with the possibility that the dissociation rates of the *Arc* RETF probes from RNA was greater than those of the *IP3R1* probes.

Activity-dependent rapid *Arc* transcription and transport have been reported with the *in situ* hybridization method; *Arc* mRNA appeared in the perikaryal cytoplasm within 15 min, and propagated to proximal dendrites within 30 min (25, 26). The RT-PCR assay in the current study showed that the *Arc* mRNA level was increased within 20 min after TTX withdrawal. In the RETF probe experiments, the concentration of *Arc* mRNA (C_{slow}) started to increase at 20 min after TTX withdrawal in the dendrite, while in the soma this occurred at 40 min (Fig. 6). The delay in the C_{slow} increase in the cell body may be explained by photobleaching during the series of measurements: the C_{slow} time course curves of the *Arc* RETF probes may have been decreased by about 20% every 20 min as the time course of C_{slow} of the scramble probe shows. RNA degradation also contributes to the decline in the C_{slow} curve of the RETF probe. Thus, we consider that C_{slow} of the RETF probe in the soma actually started to increase 20 min after the TTX wash. Additionally, the time lag of the RETF probe to become fluorescent after RNA binding (16) should be taken into account. The absolute increments in C_{slow} in the soma and dendrites were almost the same; however, the rate of increase in the soma was smaller because the basal C_{slow} value was larger in the soma than in the dendrites. Furthermore, the decrease in C_{slow} of the scramble probe after TTX removal and that of the RETF probe without wash, both of which are attributed to photobleaching during the series of measurements, were larger at the soma than at the dendrite (Fig. 6Ba), showing that the tendency for a basal decrease was greater in the soma due to its larger irradiated volume. Thus, we consider that the true increase in C_{slow} of the *Arc* RETF probe upon TTX removal in the soma was more dampened than that in the dendrite.

While the simulation of mRNA diffusion showed that free diffusion of RNA was not sufficient to bring RNA molecules to distal dendrites within a reasonable time, newly synthesized *Arc* mRNAs appeared in distal tips of the dendrite, about 300 μm from the soma, within 60 min (25, 26). MS2-labeled *β-actin* mRNAs moved in various patterns, including stationary, corralled, diffusive, and directed motion (7). Indeed, the velocity of actively transported exogenously expressed mRNA containing the 3′-UTR of *Arc* mRNA was sufficiently high to be translocated to distal dendrites rapidly (32). Given these findings, our results would support the idea that free diffusion is not capable of transporting mRNAs of sizes close to *Arc* or *IP3R* to distal dendrites (2, 54–56).

Through this study, shortcomings of the method, combination of RETF probe and FCS, have emerged as follows:

1. Not negligible amount of fluorescent RETF probes are released from target mRNA, which prevent visualizing each mRNA as a dot by masking the RNA-bound RETF probe signal (Fig. 1). The MS2 and molecular beacon systems enable visualization of mRNA particles and thus single particle tracking to quantify diffusion coefficients of labeled RNA by adding repeats of probe-binding sequence to target RNA (6, 12). For the RETF probe method, FCS is necessary for analyzing diffusion properties of labeled RNA. The dissociation of RETF probe from target RNA may be minimized by optimizing the binding sequence length for better separation of RNA-bound RETF probes from free ones.

2. Intracellular FCS accompanies slowly diffusing components presumably due to non-

specific bindings and other unknown factors (19, 43, 44) as was also seen with the scramble probe in this study. These slow components overlap with the diffusion of the RETF probe-RNA complex, making estimation of the RNA diffusion parameters difficult. In this study, the rapid *Arc* mRNA production by neuronal activation helped distinguishing RNA diffusion from other diffusion fractions.

3. The RETF probe method requires turning-on of non-fluorescent fluorophores to fluorescent by chemical reaction. At present, only fluorescein is available for the mechanism. The weak photostability of fluorescein results in the apparent photobleaching in intracellular FCS measurement. Development of next generation RETF probes with more photostable chromophores is awaited.

And this method provides the following advantages:

1. The RETF probe technique enables observation of the native movement and amount of mRNA in living cells. Fluorescence *in situ* hybridization (FISH) enables observation of mRNA localization and estimation of copy number of mRNA (57, 58), however it cannot report temporal changes but only a snapshot of mRNA localization and quantity because of tissue fixation. Live RNA imaging techniques are superior to it in obtaining temporal insights into the RNA dynamics and regulation of RNA such as biosynthesis, processing and intracellular transport. By combining with FCS, the behavior of the very low concentration, low nanomolar-order, of endogenous mRNA could be investigated, whereas precise measurement of the absolute concentration is hindered by the artifacts peculiar to intracellular FCS.

2. Endogenous mRNA can be monitored without alteration of the sequence by the RETF probe-FCS method, while other live RNA imaging techniques require addition of probe binding sequences to the target RNA sequence. In the MS2 system, aptamer-binding sequence is added to target RNA. The molecular beacon method requires fusion of long probe binding sequence repeats to the target RNA sequence when visualizing single RNA molecules. The difficulty in quantitative control of exogenous RNA expression is another issue of these methods. Singer's group created knock-in mouse lines for endogenous *β-actin* and *Arc* mRNAs to contain aptamer-binding sequences to avoid this problem; however, this solution is expensive and time-consuming.

3. A pair of chromophore- and reducing reagent-conjugated oligonucleotide probes is sufficient for the quantification of RNA dynamics. To obtain sufficiently high S/B values, the other methods usually use multiple probes per RNA (12, 59). In the MS2 and molecular beacon systems, a long repeat of probe binding sequence is fused to the target RNA and many fluorescent probes bind to it, which may affect the measurements of RNA dynamics, as the diffusion coefficient depends on the shape of molecule. While these approaches have been successful in visualizing single mRNA molecules, it is better to minimize the number of tags per RNA molecule, as bound tags may disrupt the natural conformation of the target mRNA.

In summary, we combined the RETF probe technique and FCS to establish a method for analyzing the dynamics of endogenous unmodified mRNA in living neurons. This study demonstrates that free RETF probes can be segregated from RNA-bound forms by the difference in the diffusion coefficient together with concentration estimation at the low-nanomolar range. And limitations of this method emerged including that not absolute RNA concentration but relative changes in

RNA concentration can be estimated due to nonspecific binding of RETF probes.

EXPERIMENTAL PROCEDURES

Animal care and neuron culture

Animal care was in accordance with the guidelines outlined by the Institutional Animal Care and Use Committee of Waseda University. Throughout the experimental procedures, all efforts were made to minimize the number of animals used and their suffering. Primary cultured neurons were prepared from embryos of Wistar rats on day 18 (E18), in accordance with a standard protocol (60) with modifications. Triturated neurons were plated at a density of 1.7×10^4 cells/cm^2 onto circular glass coverslips (12-mm in diameter; CD12001, Matsunami Glass, Osaka, Japan) coated with 4% polyethylenimine (P3143, Sigma-Aldrich, Tokyo, Japan), which were set in 24-well plastic dishes (92424, TPP Techno Plastic Products, Trasadingen, Switzerland), in plating medium consisting of modified Eagle's medium (MEM) supplemented with 2 mM L-glutamine, 1 mM sodium pyruvate, and 10% horse serum. After incubation for 3 days, the medium was changed to maintenance medium consisting of Neurobasal-A medium (12349-015, Gibco, Grand Island, NY, USA) supplemented with 2% B27 (17504-044, Gibco), 2 mM L-glutamine, and 0.05% penicillin/streptomycin. Primary cultured neurons at 15–20 days *in vitro* (DIV) were used.

In the electrophysiology and FCS experiments, coverslips on which neurons adhered were mounted in a stainless chamber (SCC-D35, Tokai Hit, Fujinomiya, Japan) that allows the bottom side of the coverslip facing objective directly and the top side immersed with extracellular solution. Alternatively, disposable glass-bottomed plastic dishes can be used, where weight on the top of the dish may be necessary to gain stable focus. HBS (20 mM HEPES, 115 mM NaCl, 5.4 mM KCl, 1 mM $MgCl_2$, 2 mM $CaCl_2$, and 10 mM glucose, pH 7.4) was used as an extracellular solution at room temperature throughout experiments, in which neurons were kept healthy within at least 2 h. If cells are needed to be kept for longer periods in experiment chambers, HEPES-supplemented Neurobasal-A with B27 is recommended (60).

In neuron activation experiments, neural activity was suppressed with 2 μM TTX (L8503; Latoxan, Valence, France) for 2 days before the experiment. For the induction of *Arc* mRNA, cells were washed five times with TTX-free HBS.

Electrophysiology

Probes were loaded with the whole-cell patch clamp method at room temperature. HBS was used as the external solution. Patch pipettes (6–9 MΩ) pulled from borosilicate glass capillaries (Sutter Instrument, Novato, CA, USA) were filled with the internal solution: 65 mM potassium gluconate, 65 mM Cs-methanesulfonate, 10 mM KCl, 1 mM $MgCl_2$, 4 mM Na_2ATP, 20 mM HEPES, and 0.4 mM EGTA, pH 7.3, 295 mOsm. On the day of the experiment, 2 or 10 μM RETF probe, or 0.5 μM scramble probe, and 5 μM Alexa Fluor 594 biocytin (A12922; Life Technologies Japan, Tokyo, Japan) were added to the internal solution. Whole-cell mode patch-clamps were performed using an Axopatch 1D amplifier (Molecular Devices, Sunnyvale, CA, USA). Neurons were voltage-clamped at −60 mV for 20 min to allow the probes to fill the cell, and then the pipette was removed gently to let the hole on the plasma membrane reseal: pipettes were pulled up very slowly until the tip of pipette was visibly detached from the surface of target neuron.

Quantitative RT-PCR

Total RNA was extracted with the TRIzol method (Invitrogen Japan, Tokyo, Japan) at each time point after the TTX wash out. Total RNA (0.2 μg) was reverse-transcribed to complementary DNA using ReverTra Ace qPCR RT Master Mix with a genomic DNA remover (Toyobo, Osaka, Japan), in accordance with the manufacturer's protocol. Quantitative PCR was performed with the StepOnePlus system (Applied Biosystems, Foster City, CA, USA) using THUNDERBIRD SYBR qPCR Mix (Toyobo). The relative expression level of *Arc* mRNA was normalized by that of *GAPDH* mRNA. Primers used for amplification were the same as in a previous study (47): 5′-ATCCTGCAGATTGGTAAGTGCCGA-3′ and 5′-GCACATAGCCGTCCAAGTTGTTCT-3′ for *Arc* mRNA, and 5′-AGAGACAGCCGCATCTTCTTG-3′ and 5′-GGTAACCAGGCGTCCGATAC-3′ for *GAPDH* mRNA.

Imaging

For time-lapse imaging, neurons were placed on an inverted fluorescence microscope (IX-81; Olympus, Tokyo, Japan). Fluorescence excited at 470–490 nm was acquired with a 40× objective (UPlanFL N, N.A. 0.75; Olympus) through a 500–550-nm band-pass filter using a CCD camera (C4742-95-12ERG; Hamamatsu Photonics, Hamamatsu, Japan). Confocal images were obtained using a confocal laser scanning microscope (FV-300; Olympus) equipped with a water immersion objective lens (UPlanSApo, N.A. 1.2, 60×; Olympus). RETF probes were excited with a 488-nm argon-ion laser (IMA 10×; Melles Griot, Carlsbad, CA, USA) or diode laser (STRADUS 488-25; Vortran, Sacramento, CA, USA), and detected through a 510–540-nm band-pass filter. Alexa 594 biocytin was excited using a 561-nm diode pumped solid state (DPSS) laser (85-YCA-010-040; Melles Griot), and the fluorescence was detected through a 610-nm long pass filter. Images with RETF probes and Alexa590 biocytin were taken separately with respective lasers. Confocal images were taken with Fluoview software (Olympus) bundled with the FV-300 confocal microscope system, and resultant TIFF-format image files were transferred to a Mac computer for further analysis including dendrite size measurement.

Size of dendrites

The dendritic width was determined by the line profile of fluorescence intensity orthogonal to each dendrite taken from Alexa 594 biocytin confocal images of the target neurons of the FCS measurement. A theoretical line profile of cytosolic fluorescence intensity presupposing a circular cross section of dendrite, $S(y)$, was developed by Gennerich and Schild (19):

$$S(y) = \theta exp\left[-2(y-y_0)^2/r_{xy}^2\right]\int_0^R dr\int_0^{2\pi} d\varphi\, r \times exp\left[-2\left\{\begin{matrix} r^2\cos^2\varphi - 2(y-y_0)r\cos\varphi \\ +r^2\sin^2\varphi/\gamma^2 \end{matrix}\right\}/r_{xy}^2\right]$$

with $y = y_0$ and $z = 0$ being the center of the circular cross section, the radial radius of the confocal volume $r_{xy} = 0.34$, structure factor $\gamma = r_z/r_{xy} = 9.6$, where r_z is the focal axial radius and the fitting parameter θ. Methods to deduce r_{xy} and γ are described in the following section. The dendritic radius R, y_0, and θ were obtained by fitting the dendritic profile of Alexa 594 biocytin to the model. The measurement points on the dendrite were positioned 30–50 μm away from the soma to be orthogonal to the dendrites on confocal fluorescent images of Alexa 594 biocytin. Dendritic widths were measured at two to three points in each cell. Data analyses were implemented and

performed in in-house software, TI Workbench, running on Mac computers (61).

RETF probe design

RETF probes were synthesized as previously described (16). Pairs of 15-mer oligonucleotides were modified at the 5′-terminal of one of the pair with TPP and at the 3′-terminal of the other one with Az. The sequences of the RETF probes were complementary to *Arc* mRNA: target 1, 5′-CAGCTTCCTGGCAGT-(Az) (TPP)-AGGGCTCTGGACCCC-3′; target 2, 5′-GCCGCCGGTCGTCAT-(Az) (TPP)-ATGGTCCAGCTCCAT-3′; and to *Ip3r1* mRNA: target 1, 5′-GTTGGCCCCGGGCTT-(Az) (TPP)-AGCAGCTTTCCAGAA-3′; target 2, 5′-CGGCCTCCCTCCGGA-(Az) (TPP)-AGGTGGTAAAGGCTT-3′. The scramble probe consisted of a 15-mer oligonucleotide [5′ (FL)-AGTGTACTTCGAAAT-3′] conjugated to fluorescein (FL) at the 5′-terminal.

FCS system

The confocal microscope mentioned above (FV-300; Olympus) was equipped with an additional GaAsP-type photomultiplier tube (PMT, H8631-40; Hamamatsu Photonics) for FCS, of which high sensitivity is preferred for intracellular FCS where high photobleaching prohibits long duration recording. Fluorescence excited with the 488-nm laser was detected with the PMT through a 500–550-nm band-pass filter in the photon counting mode, in which each detected photon was converted into a transistor-transistor logic (TTL) voltage signal. Photon-counting is better than analog voltage output from PMT because the former is free from thermal noise. The shortcoming of the photon-counting mode is the saturation of photon-counting with high frequency photon events, however in the case of intracellular mRNA imaging with RETF probes, the low frequency of photon events did not lead to saturation. The photon events as TTL signals were fed into a counter port of a data acquisition card (PCIe-6363; National Instruments, Austin, TX, USA) running at 1 MHz, which was connected to a Mac computer running TI Workbench. TI Workbench stored the incoming photon signals as a time series of number of events per 1 μs (61).

Intracellular FCS measurements and analysis

The recording point for FCS was positioned at the cytosol in the somata or dendrites 30–50 μm away from the soma, guided by the Alexa 594 biocytin fluorescence. The z-position was set to positions where the signal of Alexa 594 biocytin was maximal. The recording mode of the Fluoview software, running on a Windows PC, was switched from the 2D image acquisition mode to the point-scan mode, and recording point was set on the 2D image on computer screen. The light path for fluorescence was switched to the additional PMT for FCS and the point-scan mode recording was started in the Fluoview software. TI Workbench on a Mac computer started recording through the additional PMT by receiving a TTL trigger from the FV-300 confocal system.

FCS measurement was performed at a single point for 20 s, which was repeated 5–12 times at the same point. Autocorrelation function of each 20 s recording was calculated separately as described below, and autocorrelation functions recorded from the same recording point were averaged to avoid slow fluorescence decay of time constants longer than several seconds arising from photobleaching of diffusing molecules within the diffusion compartment, which would have occurred if the recording and autocorrelation calculation was not divided and then averaged

but done continuously in living cells (43).

To further compensate for the photobleaching effects, intensity traces were corrected before calculating the autocorrelation function. The fluorescence intensity time course, $I(t)$, was fitted to a two-component exponential function, which accounts for fast and slow photobleaching:

$i(t) = i_0 + i_1 \cdot \exp(t/t_{B1}) + i_2 \cdot \exp(t/t_{B2})$. With these fitted parameters, bleach-corrected fluorescence intensity, $I_c(t)$ was calculated with the following formula:

$$I_c(t) = I(t) \cdot \frac{i(0)}{i(t)}$$

Autocorrelation functions were calculated along an exponentially interleaved delay time progression, $\tau_n = \tau_0 \cdot 10^{0.01n}$, where τ_0 is the sampling time (1 μs). τ_n ranged from 1 μs to 10 s; that is, integer n was in the range of $0 \leq n \leq 700$ in this study.

The autocorrelation function, $G(\tau) = \langle F(t) \cdot F(t+\tau) \rangle / \langle F(t) \rangle^2 - 1$, where $\langle F(t) \rangle$ is the mean fluorescence intensity of each photobleaching-corrected recording (I_c), was calculated as follows:

$$G(\tau_n) = \frac{\frac{1}{M} \cdot \sum_{k=0}^{M} \left[\left\{ \sum_{l=nk+1}^{nk+n} I_c(l\tau_0) \right\} \cdot \left\{ \sum_{l=n(k+1)+1}^{n(k+1)+n} I_c(l\tau_0) \right\} \right]}{\left\{ \frac{1}{M} \sum_{k=0}^{M} \sum_{l=nk+1}^{nk+n} I_c(l\tau_0) \right\}^2} - 1.$$

Here, M is an integer given by T/τ_n where T is the total measurement duration (20 s).

Autocorrelation functions taken from each single cell were averaged, and then fitted to a one- or two-component diffusion model, using the Levenberg–Marquardt algorithm (45, 62),

$$G(\tau) = \frac{\sum_{i=1}^{N} C_i \varepsilon_i^2 \, g_{Bi}(\tau) Trp_i(\tau)}{V_{eff} \left(\sum_{i=1}^{N} C_i \varepsilon_i \right)^2} + G_\infty$$

with

$$Trp_i(\tau) = 1 + \frac{p_{T_i}}{1 - p_{T_i}} exp\left(-\frac{\tau}{\tau_{T_i}} \right)$$

where C_i and ε_i are the concentration of the ith species and the brightness of each diffusing particle in the ith component. Fitting the autocorrelation functions with the two-component model resulted in brightness of fluorescent particles in the second (slower diffusing) component relative to that in the first (faster diffusing) component $\varepsilon_{slow}/\varepsilon_{fast}$. The $Trp_i(\tau)$ term expresses triplet–singlet transitions (63, 64). p_T is the fraction of particles in the triplet state with a delay time of τ_{Ti}.

In the three-dimensional (3D) free diffusion model, g_{Bi} is given by

$$g_{Bi}(\tau) = \frac{1}{1+\frac{\tau}{\tau_{Di}}} \cdot \frac{1}{\sqrt{1+\frac{\tau}{\gamma^2 \tau_{Di}}}} \quad (65).$$

The effective detection volume, V_{eff}, for this 3D model is given by $V_{eff} = \pi^{\frac{3}{2}} {r_{xy}}^2 r_z$.

In the case that diffusion is confined in axial and lateral directions, it is appropriate to apply a confinement diffusion model (19, 42). When the dendritic diameter, d_{dend}, is sufficiently smaller than the height of the detection volume, namely, $d_{dend}/r_z < 0.833$, the diffusion in the axial direction is negligible (42). Thus, g_{Bi} is expressed by

$$g_{Bi}(\tau) = g_{xi}(\tau) \cdot g_{yi}(\tau)$$

in such a case. If the confinement parameter $Y = d_{dend}/r_{xy}$ is smaller than 8, g_{yi} is approximated as

$$g_{xi}(\tau) = \frac{1}{\sqrt{1+\frac{\tau}{\tau_{Di}}}}, g_{yi}(\tau) = \frac{\sqrt{\pi}}{Y} \left[1 + \left(\frac{Y}{\sqrt{\pi}} - 1 \right) \frac{exp\left(-\left(\frac{0.83\pi}{Y} \right)^2 \frac{\tau}{\tau_{Di}} \right)}{\sqrt{1+\frac{\tau}{\tau_{Di}}}} \right] \quad (42),$$

and V_{eff} is given by $V_{eff} = \pi r_{xy}^2 d_{dend}$.

The singlet–triplet transition was corrected by setting a constant value τ_T, which was deduced to be 23 μs for intracellular measurements of the RETF probes, 18 μs for

intracellular measurements of the scramble probe, and 10 μs for the scramble probe in cell-free measurements after fitting the averaged autocorrelation curves of each probe. The diffusion coefficient D_i was calculated by

$$D_i = \frac{{r_{xy}}^2}{4\tau_{Di}}.$$

Simulation

Diffusion simulation was performed based on the Fick–Jacobs equation (66), representing a 1D diffusion model in a cylindrical tube of varying cross-sectional area. Directing the x-axis along the tube and denoting the cross-sectional area at x by $S(x)$ with RNA degradation constant γ_{rna}, the effective 1D concentration $C(x,t)$ was given by the Fick–Jacobs equation:

$$\frac{\partial C(x,t)}{\partial t} = D\frac{\partial}{\partial x}\left\{S(x)\frac{\partial}{\partial x}\left[\frac{C(x,t)}{S(x)}\right]\right\} - \gamma_{rna}C(x,t)$$

$$= D\frac{\partial^2}{\partial x^2}C(x,t) - D\frac{\partial}{\partial x}\left(\frac{S'(x)}{S(x)}\cdot C(x,t)\right) - \gamma_{rna}C(x,t),$$

where D is the diffusion coefficient. To simplify the cross-sectional change in the dendrite, $S(x)$ was imposed according to Rall's 3/2 power law (67): $DIA^{3/2} = \sum dia^{3/2}$, which describes the relationship between the diameter of the parent (*DIA*) and daughter (*dia*) branches. When the cross-sectional area of the branch was calculated based on Rall's law, the sum of the daughter cross-sectional area was reduced by approximately 20% of the mother cross-sectional area at every bifurcation point. The change in cross-sectional area was formulated as $S(x) = 0.8^{bn\cdot x/L}$, where L is the dendrite length and *bn* represents the total bifurcation number. In this simulation, both parameters were set as L = 300 μm and *bn* = 16. The degradation rate γ_{rna} was *log(2)/ht*, where the half-life *ht* was set as 47 min (46). As the particles cannot escape from the tip of a dendrite, the boundary condition at x = L was $\partial C(L,t)/\partial x = 0$. At the dendrite base (x = 0), the concentration was increased linearly within 40 min to match the result of the gene induction experiment by the RT-PCR assay. That is, $C(0,t) = 0.025t$ for $0 \le t \le 40$ min and $C(0,t) = 1$ for $40 < t$ min. The simulation was performed on Python.

Concentrations of RNA and RETF probe in equilibrium

The equilibrium dissociation constant (K_D) of the RNA-RETF probe binding is calculated as

$$K_D = \frac{[RNA_{free}]\cdot[RETF_{free}]}{[RNA_{bound}]},$$

where free RNA concentration ($[RNA_{free}]$), free RETF probe concentration ($[RETF_{free}]$), and RETF probe-bound RNA concentration ($[RNA_{bound}]$). Using the relations, $[RNA_{total}] = [RNA_{bound}] + [RNA_{free}]$, $[RETF_{total}] = [RETF_{bound}] + [RETF_{free}]$, and $[RETF_{bound}] = [RNA_{bound}]$, the K_D formula is rearranged to

$$[RNA_{total}] = [RNA_{bound}]\cdot\frac{[RETF_{total}] - [RNA_{bound}] + K_D}{[RETF_{total}] - [RNA_{bound}]}.$$

Statistics

All offline analyses were performed using the in-house software, TI Workbench, running on a Mac computer in combination (61) with Microsoft Excel (Microsoft Japan, Tokyo, Japan), R (Vienna University of Economics and Business), and Igor Pro (Wavemetrics, Lake Oswego, OR, USA). Indicated data are given as "median (first quartile–third quartile)" or "average ± standard deviation (s.d.)" unless otherwise indicated.

DATA AVAILABILITY

The data that support the findings of this study are available from the corresponding author upon reasonable request.

ACKNOWLEDGEMENTS

This work was supported by Grant-in-Aid for Scientific Research from the Japan Society for the Promotion of Science [JSPS; 23300121 and 26640016 (T.I.)], Private University Research Branding Project (MEXT, Japan, T.I.), and Waseda University Grants for Special Research Projects. The authors thank Edanz (www.edanzediting.co.jp) for editing the English text of a draft of this manuscript. All of the authors declare no conflicts of interest in this study.

CONFLICT OF INTEREST

The authors declare that they have no conflicts of interest with the contents of this article.

REFERENCES

1. Doyle, M., and Kiebler, M. A. (2011) Mechanisms of dendritic mRNA transport and its role in synaptic tagging. *EMBO J.* **30**, 3540–3552
2. Bramham, C. R., and Wells, D. G. (2007) Dendritic mRNA: transport, translation and function. *Nat. Rev. Neurosci.* **8**, 776–789
3. Glock, C., Heumüller, M., and Schuman, E. M. (2017) mRNA transport & local translation in neurons. *Curr. Opin. Neurobiol.* **45**, 169–177
4. Holt, C. E., Martin, K. C., and Schuman, E. M. (2019) Local translation in neurons: visualization and function. *Nat. Struct. Mol. Biol.* **26**, 557–566
5. Urbanek, M. O., Galka-Marciniak, P., Olejniczak, M., and Krzyzosiak, W. J. (2014) RNA imaging in living cells - methods and applications. *RNA Biol.* **11**, 1083–1095
6. Bertrand, E., Chartrand, P., Schaefer, M., Shenoy, S. M., Singer, R. H., and Long, R. M. (1998) Localization of ASH1 mRNA particles in living yeast. *Mol. Cell*. **2**, 437–445
7. Park, H. Y., Lim, H., Yoon, Y. J., Follenzi, A., Nwokafor, C., Lopez-Jones, M., Meng, X., and Singer, R. H. (2014) Visualization of dynamics of single endogenous mRNA labeled in live mouse. *Science*. **343**, 422–424
8. Das, S., Moon, H. C., Singer, R. H., and Park, H. Y. (2018) A transgenic mouse for imaging activity-dependent dynamics of endogenous Arc mRNA in live neurons. *Sci. Adv.* **4**, eaar3448
9. Ozawa, T., Natori, Y., Sato, M., and Umezawa, Y. (2007) Imaging dynamics of endogenous mitochondrial RNA in single living cells. *Nat. Methods*. **4**, 413–419
10. Yamada, T., Yoshimura, H., Shimada, R., Hattori, M., Eguchi, M., Fujiwara, T. K., Kusumi, A., and Ozawa, T. (2016) Spatiotemporal analysis with a genetically encoded fluorescent RNA probe reveals TERRA function around telomeres. *Sci. Rep.* **6**, 38910
11. Tyagi, S., and Kramer, F. R. (1996) Molecular Beacons: Probes that Fluoresce upon Hybridization. *Nat. Biotechnol.* **14**, 303–308
12. Vargas, D. Y., Raj, A., Marras, S. A. E., Kramer, F. R., and Tyagi, S. (2005) Mechanism of mRNA transport in the nucleus. *Proc. Natl. Acad. Sci. U. S. A.* **102**, 17008–17013
13. Nelles, D. A., Fang, M. Y., O'Connell, M. R., Xu, J. L., Markmiller, S. J., Doudna, J. A., and Yeo, G. W. (2016) Programmable RNA Tracking in Live Cells with CRISPR/Cas9. *Cell*. **165**, 488–496
14. Turner-Bridger, B., Jakobs, M., Muresan, L., Wong, H. H.-W., Franze, K., Harris, W. A., and Holt, C. E. (2018) Single-molecule analysis of endogenous β-actin mRNA trafficking reveals a mechanism for compartmentalized mRNA localization in axons. *Proc. Natl. Acad. Sci. U. S. A.* **115**, E9697–E9706
15. Abe, H., Wang, J., Furukawa, K., Oki, K., Uda, M., Tsuneda, S., and Ito, Y. (2008) A reduction-triggered fluorescence probe for sensing nucleic acids. *Bioconjug. Chem.* **19**, 1219–1226
16. Furukawa, K., Abe, H., Hibino, K., Sako, Y., Tsuneda, S., and Ito, Y. (2009) Reduction-triggered fluorescent amplification probe for the detection of endogenous RNAs in living human cells. *Bioconjug. Chem.* **20**, 1026–1036
17. Furukawa, K., Abe, H., Tamura, Y., Yoshimoto, R., Yoshida, M., Tsuneda, S., and

Ito, Y. (2011) Fluorescence detection of intron lariat RNA with reduction-triggered fluorescent probes. *Angew. Chem. Int. Ed Engl.* **50**, 12020–12023
18. Marras, S. A. E., Kramer, F. R., and Tyagi, S. (2002) Efficiencies of fluorescence resonance energy transfer and contact-mediated quenching in oligonucleotide probes. *Nucleic Acids Res.* **30**, e122
19. Gennerich, A., and Schild, D. (2002) Anisotropic diffusion in mitral cell dendrites revealed by fluorescence correlation spectroscopy. *Biophys. J.* **83**, 510–522
20. Chen, J.-H., Kellner, Y., Zagrebelsky, M., Grunwald, M., Korte, M., and Walla, P. J. (2015) Two-Photon Correlation Spectroscopy in Single Dendritic Spines Reveals Fast Actin Filament Reorganization during Activity-Dependent Growth. *PLOS ONE*. **10**, e0128241
21. Wu, B., Chao, J. A., and Singer, R. H. (2012) Fluorescence fluctuation spectroscopy enables quantitative imaging of single mRNAs in living cells. *Biophys. J.* **102**, 2936–2944
22. Wu, B., Buxbaum, A. R., Katz, Z. B., Yoon, Y. J., and Singer, R. H. (2015) Quantifying protein-mRNA interactions in single live cells. *Cell*. **162**, 211–220
23. Link, W., Konietzko, U., Kauselmann, G., Krug, M., Schwanke, B., Frey, U., and Kuhl, D. (1995) Somatodendritic expression of an immediate early gene is regulated by synaptic activity. *Proc. Natl. Acad. Sci. U. S. A.* **92**, 5734–5738
24. Lyford, G. L., Yamagata, K., Kaufmann, W. E., Barnes, C. A., Sanders, L. K., Copeland, N. G., Gilbert, D. J., Jenkins, N. A., Lanahan, A. A., and Worley, P. F. (1995) Arc, a growth factor and activity-regulated gene, encodes a novel cytoskeleton-associated protein that is enriched in neuronal dendrites. *Neuron*. **14**, 433–445
25. Wallace, C. S., Lyford, G. L., Worley, P. F., and Steward, O. (1998) Differential intracellular sorting of immediate early gene mRNAs depends on signals in the mRNA sequence. *J. Neurosci. Off. J. Soc. Neurosci.* **18**, 26–35
26. Guzowski, J. F., McNaughton, B. L., Barnes, C. A., and Worley, P. F. (1999) Environment-specific expression of the immediate-early gene Arc in hippocampal neuronal ensembles. *Nat. Neurosci.* **2**, 1120–1124
27. Farris, S., Lewandowski, G., Cox, C. D., and Steward, O. (2014) Selective Localization of Arc mRNA in Dendrites Involves Activity- and Translation-Dependent mRNA Degradation. *J. Neurosci.* **34**, 4481–4493
28. Moga, D. E., Calhoun, M. E., Chowdhury, A., Worley, P., Morrison, J. H., and Shapiro, M. L. (2004) Activity-regulated cytoskeletal-associated protein is localized to recently activated excitatory synapses. *Neuroscience*. **125**, 7–11
29. Chowdhury, S., Shepherd, J. D., Okuno, H., Lyford, G., Petralia, R. S., Plath, N., Kuhl, D., Huganir, R. L., and Worley, P. F. (2006) Arc/Arg3.1 interacts with the endocytic machinery to regulate AMPA receptor trafficking. *Neuron*. **52**, 445–459
30. Ashley, J., Cordy, B., Lucia, D., Fradkin, L. G., Budnik, V., and Thomson, T. (2018) Retrovirus-like Gag Protein Arc1 Binds RNA and Traffics across Synaptic Boutons. *Cell*. **172**, 262-274.e11
31. Pastuzyn, E. D., Day, C. E., Kearns, R. B., Kyrke-Smith, M., Taibi, A. V., McCormick, J., Yoder, N., Belnap, D. M., Erlendsson, S., Morado, D. R., Briggs, J. A. G., Feschotte, C., and Shepherd, J. D. (2018) The Neuronal Gene Arc Encodes a Repurposed Retrotransposon Gag Protein that Mediates Intercellular RNA Transfer. *Cell*. **172**, 275-288.e18

32. Dynes, J. L., and Steward, O. (2007) Dynamics of bidirectional transport of Arc mRNA in neuronal dendrites. *J. Comp. Neurol.* **500**, 433–447
33. Dynes, J. L., and Steward, O. (2012) Arc mRNA docks precisely at the base of individual dendritic spines indicating the existence of a specialized microdomain for synapse-specific mRNA translation. *J. Comp. Neurol.* **520**, 3105–3119
34. Furuichi, T., Simon-Chazottes, D., Fujino, I., Yamada, N., Hasegawa, M., Miyawaki, A., Yoshikawa, S., Guénet, J. L., and Mikoshiba, K. (1993) Widespread expression of inositol 1,4,5-trisphosphate receptor type 1 gene (Insp3r1) in the mouse central nervous system. *Receptors Channels*. **1**, 11–24
35. Inoue, T., Kato, K., Kohda, K., and Mikoshiba, K. (1998) Type 1 Inositol 1,4,5-Trisphosphate Receptor Is Required for Induction of Long-Term Depression in Cerebellar Purkinje Neurons. *J. Neurosci.* **18**, 5366–5373
36. Itoh, S., Ito, K., Fujii, S., Kaneko, K., Kato, K., Mikoshiba, K., and Kato, H. (2001) Neuronal plasticity in hippocampal mossy fiber-CA3 synapses of mice lacking the inositol-1,4,5-trisphosphate type 1 receptor. *Brain Res.* **901**, 237–246
37. Fujii, S., Matsumoto, M., Igarashi, K., Kato, H., and Mikoshiba, K. (2000) Synaptic plasticity in hippocampal CA1 neurons of mice lacking type 1 inositol-1,4,5-trisphosphate receptors. *Learn. Mem. Cold Spring Harb. N.* **7**, 312–320
38. Bannai, H., Fukatsu, K., Mizutani, A., Natsume, T., Iemura, S.-I., Ikegami, T., Inoue, T., and Mikoshiba, K. (2004) An RNA-interacting protein, SYNCRIP (heterogeneous nuclear ribonuclear protein Q1/NSAP1) is a component of mRNA granule transported with inositol 1,4,5-trisphosphate receptor type 1 mRNA in neuronal dendrites. *J. Biol. Chem.* **279**, 53427–53434
39. Savas, J. N., Ma, B., Deinhardt, K., Culver, B. P., Restituito, S., Wu, L., Belasco, J. G., Chao, M. V., and Tanese, N. (2010) A role for huntington disease protein in dendritic RNA granules. *J. Biol. Chem.* **285**, 13142–13153
40. Kinjo, M., Sakata, H., and Mikuni, S. (2010) First Steps for Fluorescence Correlation Spectroscopy of Living Cells. in *Live Cell Imaging*, second edition, pp. 229–238, Cold Spring Harbor Laboratory Press, New York
41. Müller, C. B., Loman, A., Pacheco, V., Koberling, F., Willbold, D., Richtering, W., and Enderlein, J. (2008) Precise measurement of diffusion by multi-color dual-focus fluorescence correlation spectroscopy. *EPL*. **83**, 46001
42. Gennerich, A., and Schild, D. (2000) Fluorescence correlation spectroscopy in small cytosolic compartments depends critically on the diffusion model used. *Biophys. J.* **79**, 3294–3306
43. Pack, C., Saito, K., Tamura, M., and Kinjo, M. (2006) Microenvironment and effect of energy depletion in the nucleus analyzed by mobility of multiple oligomeric EGFPs. *Biophys. J.* **91**, 3921–3936
44. Wachsmuth, M., Waldeck, W., and Langowski, J. (2000) Anomalous diffusion of fluorescent probes inside living cell nuclei investigated by spatially-resolved fluorescence correlation spectroscopy. *J. Mol. Biol.* **298**, 677–689
45. Heidarinejad, M., Nakamura, H., and Inoue, T. (2018) Stimulation-induced changes in diffusion and structure of calmodulin and calmodulin-dependent protein kinase II proteins in neurons. *Neurosci. Res.* **136**, 13–32
46. Rao, V. R., Pintchovski, S. A., Chin, J., Peebles, C. L., Mitra, S., and Finkbeiner, S. (2006) AMPA receptors regulate transcription of the plasticity-related immediate-early gene Arc. *Nat. Neurosci.* **9**, 887–895

47. Saha, R. N., Wissink, E. M., Bailey, E. R., Zhao, M., Fargo, D. C., Hwang, J.-Y., Daigle, K. R., Fenn, J. D., Adelman, K., and Dudek, S. M. (2011) Rapid activity-induced transcription of Arc and other IEGs relies on poised RNA polymerase II. *Nat. Neurosci.* **14**, 848–856
48. Mikl, M., Vendra, G., and Kiebler, M. A. (2011) Independent localization of MAP2, CaMKIIα and β-actin RNAs in low copy numbers. *EMBO Rep.* **12**, 1077–1084
49. Eliscovich, C., Buxbaum, A. R., Katz, Z. B., and Singer, R. H. (2013) mRNA on the move: the road to its biological destiny. *J. Biol. Chem.* **288**, 20361–20368
50. Medioni, C., Mowry, K., and Besse, F. (2012) Principles and roles of mRNA localization in animal development. *Dev. Camb. Engl.* **139**, 3263–3276
51. Walton, S. P., Stephanopoulos, G. N., Yarmush, M. L., and Roth, C. M. (2002) Thermodynamic and kinetic characterization of antisense oligodeoxynucleotide binding to a structured mRNA. *Biophys. J.* **82**, 366–377
52. Fusco, D., Accornero, N., Lavoie, B., Shenoy, S. M., Blanchard, J.-M., Singer, R. H., and Bertrand, E. (2003) Single mRNA molecules demonstrate probabilistic movement in living mammalian cells. *Curr. Biol. CB*. **13**, 161–167
53. Lifland, A. W., Zurla, C., Yu, J., and Santangelo, P. J. (2011) Dynamics of native β-actin mRNA transport in the cytoplasm. *Traffic Cph. Den.* **12**, 1000–1011
54. Carson, J. H., Cui, H., and Barbarese, E. (2001) The balance of power in RNA trafficking. *Curr. Opin. Neurobiol.* **11**, 558–563
55. Hirokawa, N. (2006) mRNA transport in dendrites: RNA granules, motors, and tracks. *J. Neurosci. Off. J. Soc. Neurosci.* **26**, 7139–7142
56. Kiebler, M. A., and Bassell, G. J. (2006) Neuronal RNA granules: movers and makers. *Neuron*. **51**, 685–690
57. Femino, A. M., Fay, F. S., Fogarty, K., and Singer, R. H. (1998) Visualization of single RNA transcripts in situ. *Science*. **280**, 585–590
58. Raj, A., van den Bogaard, P., Rifkin, S. A., van Oudenaarden, A., and Tyagi, S. (2008) Imaging individual mRNA molecules using multiple singly labeled probes. *Nat. Methods*. **5**, 877–879
59. Raj, A., Peskin, C. S., Tranchina, D., Vargas, D. Y., and Tyagi, S. (2006) Stochastic mRNA synthesis in mammalian cells. *PLoS Biol.* **4**, e309
60. Bannai, H., Lévi, S., Schweizer, C., Inoue, T., Launey, T., Racine, V., Sibarita, J.-B., Mikoshiba, K., and Triller, A. (2009) Activity-dependent tuning of inhibitory neurotransmission based on GABAAR diffusion dynamics. *Neuron*. **62**, 670–682
61. Inoue, T. (2018) TI Workbench, an integrated software package for electrophysiology and imaging. *Microscopy*. **67**, 129–143
62. Wohland, T., Rigler, R., and Vogel, H. (2001) The standard deviation in fluorescence correlation spectroscopy. *Biophys. J.* **80**, 2987–2999
63. Widengren, J., Mets, U., and Rigler, R. (1995) Fluorescence correlation spectroscopy of triplet states in solution: a theoretical and experimental study. *J. Phys. Chem.* **99**, 13368–13379
64. Shin, H.-S., Okamoto, A., Sako, Y., Kim, S. W., Kim, S. Y., and Pack, C.-G. (2013) Characterization of the triplet state of hybridization-sensitive DNA probe by using fluorescence correlation spectroscopy. *J. Phys. Chem. A*. **117**, 27–33
65. Rigler, R., Mets, Ü., Widengren, J., and Kask, P. (1993) Fluorescence correlation spectroscopy with high count rate and low background: analysis of translational

diffusion. *Eur. Biophys. J.* **22**, 169–175
66. Jacobs, M. H. (1967) *Diffusion Processes*, Springer, New York
67. Rall, W. (1959) Branching dendritic trees and motoneuron membrane resistivity. *Exp. Neurol.* **1**, 491–527

FOOTNOTES

The abbreviations used are: Arc, activity-regulated cytoskeleton protein; Az, azidomethyl fluorescein; C, concentration; D, diffusion constant; FCS, fluorescence correlation spectroscopy; IP3R1 inositol 1,4,5-trisphosphate receptor type 1; K_D, equilibrium dissociation constant; RETF, reduction-triggered fluorescence; S/B, signal-to-background ratio; TPP, tripheniylphosphine; TTX, tetrodotoxin; UTR, untranslated region.

Figure Legend

Figure 1. Temporal changes and distribution of fluorescence derived from RETF probes.

(A) The mechanism of RETF probe. The azidomethyl modification of fluorescein (F) hinders its fluorescence emission, which is recovered by the reduction reaction by TPP (15). (B) Time lapse images of hippocampal neurons loaded with RETF probes targeting *Arc* or *Ip3r1* mRNA, or a mismatched pair of RETF probes targeting *Arc* mRNA after forming a whole-cell patch clamp. In the mismatched RETF probe set, the Az probe of target 1 and the TPP probe of target 2 *Arc* RETF probes were used. Scale bar, 20 μm. (C) Time course of relative changes in fluorescence intensity of the *Arc* target 1 (3 cells) and *Ip3r1* target 1 (3 cells) RETF probes, the scramble probe (3 cells) and a mismatched RETF probe (4 cells) in soma (left) and dendrites (right). Means ± s.d. are indicated by error bars. $*p < 0.05$, $**p < 0.01$, $***p < 0.001$; assessed by two-way repeated ANOVA between the mismatch and each probe. (D) Fluorescence images of neurons filled with Alexa Fluor 594 Biocytin and RETF probes targeting *Arc* (left) *and Ip3r1* (right) mRNA. Scale bar, 20 μm.

Figure 2. Schematic drawing of FCS measurement and analysis

(A) Calibrations of the FCS measurement system. Laser power adjustment (a) and focal volume calibration (b) should be done periodically. (B) Procedure of data acquisition; (a) RETF probes or the scramble probe together with a marker dye, Alexa 594 biocytin, were loaded to neurons with the whole-cell patch clamp method (details in the *Electrophysiology* subsection in Experimental Procedures). (b) A confocal image of Alexa 594 biocytin was taken with a 561 nm laser for the determination of dendritic width. (c) A recording points was chosen and irradiated with 488 nm laser at the same laser power as used in FCS measurements for 5 sec. (d) 20 s FCS records were repeated for several times at the same point. Step (d) was repeated in the neuron stimulation experiments, and steps (c) and (d) were repeated several times in other experiments (details in the *FCS measurements and analysis* subsection in Experimental Procedures). (C) FCS analysis; (a) Dendritic size of the measurement positions was determined using the confocal images, and parameters for the confined diffusion model was calculated for dendritic FCS measurements (details in the *Size of dendrites* subsection in Experimental Procedures). (b) Photobleaching of raw fluorescence intensity traces were assessed and corrected. (c) Autocorrelation function (ACF) was calculated from each corrected intensity trace. ACFs taken from each cell were averaged. Diffusion parameters in each cell were obtained by fitting with diffusing models to the average of ACF of each cell (details in the *FCS measurements and analysis* subsection in Experimental Procedures).

Figure 3. Width of dendrites

(A) (left image) A confocal image of a neuron with Alexa 594 biocytin. Along the red line over a dendrite 30–50 μm away from the soma, fluorescence intensity distribution was measured (black trace in the right graph), to which a theoretical line profile of cytosolic fluorescence intensity

presupposing a circular cross section was fitted (broken red trace, $\theta = 3.5$ counts/μm^2, $R = 1.3$ μm, $y_0 = 3.4$ μm, see Experimental Procedures). Scale bar: 20 μm. (B) Diameter of dendrites of neurons. Radii of dendrites were measured at two to three points and averaged in each neuron in which FCS measurement was performed (56 cells in Fig. 5).

Figure 4. Fluorescence intensity time course and autocorrelation functions

(A) Exemplifying fluorescence intensity traces with the control scramble probe and the *Arc* target 1 and *Ip3r1* target 1 RETF probes taken at dendrites are shown after resampling at 10 Hz. Inset: raw photon events sampled at 1 MHz with scale bars (2 ms and 1 MHz). (B–C) Top: representative averaged autocorrelation functions obtained in somata (B) and in dendrites (C) of single cells are fitted with one- (blue line) and two-component diffusion models (red line). A 3D diffusion model and a confined diffusion model were used for soma and dendrite, respectively. For *Arc* and *Ip3r1* probes, results with the target 1 probes are shown. The dashed red lines represent each component of the two-component fit results. Middle: residuals of the fitting. Bottom: autocorrelation functions averaged in each cell are superposed after normalization by the G(0) value deduced by the fitting.

Figure 5. Dynamics of *Arc* and *Ip3r1* mRNA-targeted RETF probes

Diffusion coefficients of the faster and the slower component (D_{fast} and D_{slow}; A–B), ratio of concentration of the slower component to that of the total concentration (C_{slow}/C_{total}; C), and the ratio of particle brightness of the slower diffusing component to that of the faster diffusing component ($\varepsilon_{slow}/\varepsilon_{fast}$; D) of the scramble probe (scr, green marks), target 1, target 2, and both target 1 and 2 of *Arc* RETF probes (represented as 1, 2, and 1&2 with red marks), and *Ip3r1* RETF probes (represented as 1, 2, and 1&2 with blue marks) were calculated by fitting averaged autocorrelation functions in neurons with a two-component 3D diffusion model. In dendrite, a two-component confined diffusion model was also used (left) in addition to the 3D model (right). Autocorrelation functions of recording series in single neurons were averaged and represented as single marks. Medians are indicated by black lines. For simplicity, not all statistical differences among groups are indicated. All data and statistical results are shown numerically in Table S1. *$p < 0.05$, **$p < 0.01$, ***$p < 0.001$; assessed by Mann–Whitney U test.

Figure 6. Activation of *Arc* transcription and changes in FCS parameters of the slower component after neural activation

(A) The expression level of *Arc* mRNA was measured by RT-PCR and normalized to that of *GAPDH* mRNA every 20 min after TTX washout (n = 3). Means ± s.d. are indicated by error bars. (B) Time course of C_{slow} (a), $\varepsilon_{slow}/\varepsilon_{fast}$ (b) and D_{slow} (c) in the soma and dendrites (n = 5 cells). Neurons were loaded with 2 or 10 μM RETF probe (target 2) or the scramble probe. The fluorescence fluctuation was measured 4–13 times for 20 s every 20 min after TTX removal. Averaged autocorrelation functions in single neurons of each time point were fitted with the two-

component diffusion model. Each dot represents the result of each single neuron. Medians are indicated by marks and connected by lines. *$p < 0.05$, **$p < 0.01$; assessed by paired *t*-test between 0 min and each time course. Data are also shown numerically in Table S2.

Figure 7. Time course of FCS parameters of the faster component after neuronal activation

Time course of concentration of the faster component (C_{fast}; A)**,** C_{fast} normalized to time 0 (B), and D_{fast} (C) in the soma and dendrites from the same experiment set shown in Fig. 6. *$p < 0.05$, **$p < 0.01$; assessed by paired *t*-test between 0 min and each time course. Data are also shown numerically in Table S2.

Figure 8. Simulation of the spread of diffusing RNA in the dendrite

(A) A compartmentalized one-dimensional diffusion model with a tapered cylindrical tube. The model dendrite was divided into compartments where the changes in the number of contained particles was determined as the net fluxes at both ends (position x_k and x_{k+1}) of tapering cross-sectional area $S(x)$. (B and C) The spread of diffusing RNA molecules was simulated with a diffusion coefficient (D_{slow} = 2.1 μm^2/s) every 20 min with (B) and without (C) the RNA degradation term. Note that the concentration at the base of the dendrite increased linearly within 40 min.

Figure 9. Dynamics of RETF probe

RETF probes emitted fluorescence after a pair of probes bound to target mRNAs (1). Some fluorescent RETF probes detached from the target mRNA (3), which diffused much faster than RETF probes bound to mRNA with a left-shifted autocorrelation function (right panel). In the case of mRNAs with a short half-life, intact mRNAs were immediately degraded into fragmented RNAs (2) with intermediate diffusion coefficients between (1) and (3).

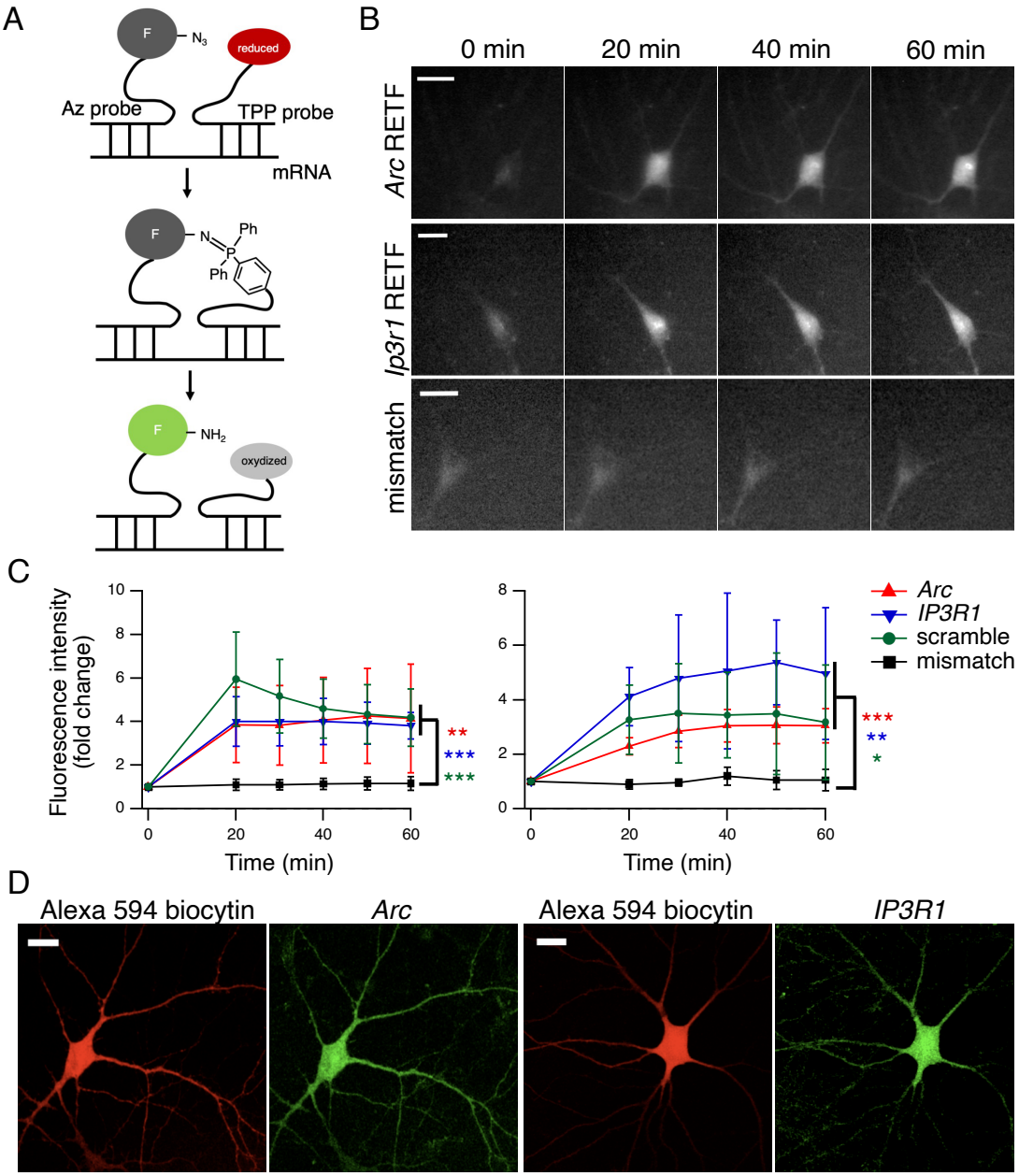
A
F
N3
reduced
Az probe
TPP probe
mRNA
Ph
Ph
NH2
oxydized
B
0 min
20 min
40 min
60 min
Arc RETF
Ip3r1 RETF
mismatch
C
Fluorescence intensity (fold change)
Time (min)
Arc
IP3R1
scramble
mismatch
D
Alexa 594 biocytin
Arc
Alexa 594 biocytin
IP3R1

Figure 1

A. Calibration (periodically)

a. laser power adjustment

b. focal volume calibration

B. Data acquisition

a. probe loading

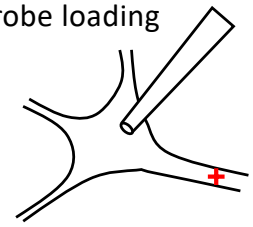

b. image capture

c. laser irradiation

d. series of FCS measurements

C. FCS analysis

a. determination of dendrite size and confined parameter *Y*

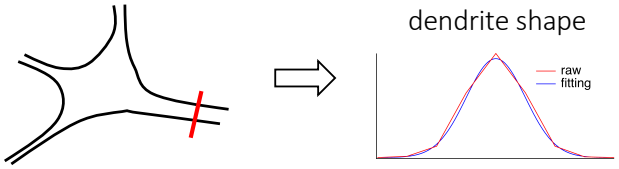

b. photobleaching correction of each 20 s record

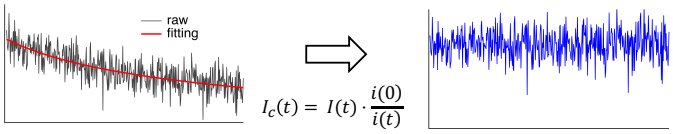

c. calculation of ACF and fitting to diffusion models

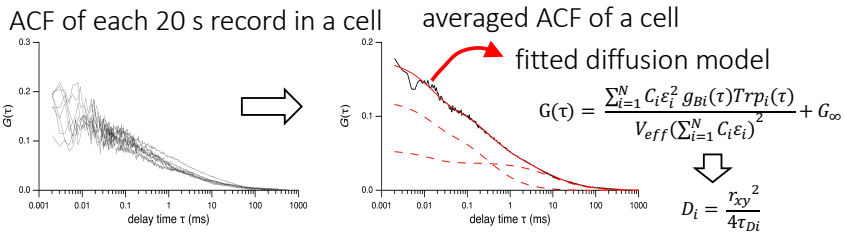

Figure 2

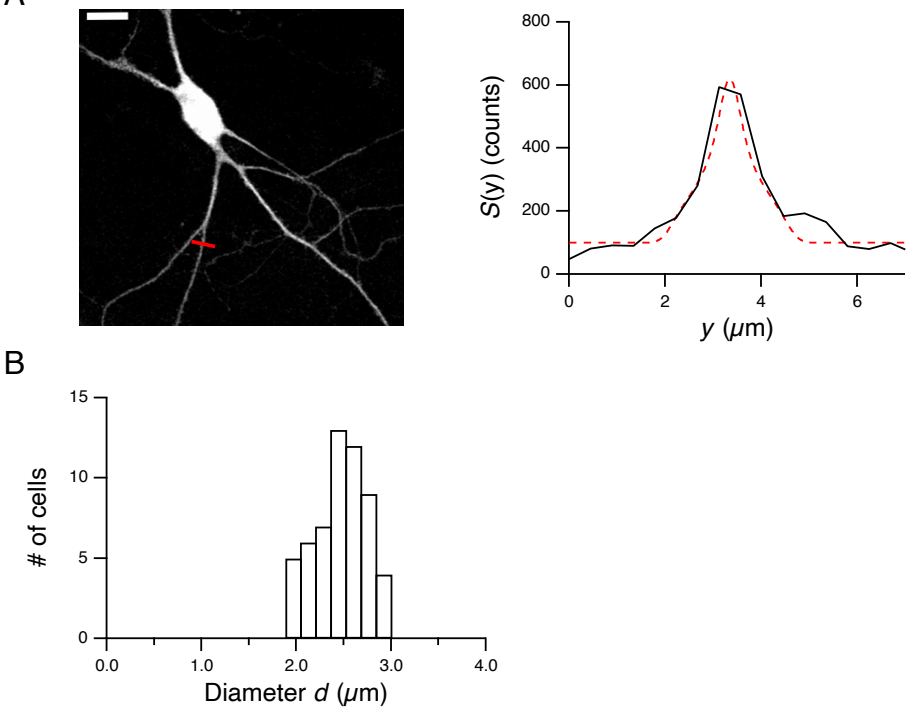
A
800
600
400
200
0
S(y) (counts)
0
2
4
6
y (μm)
B
15
10
5
0
# of cells
0.0
1.0
2.0
3.0
4.0
Diameter d (μm)

Figure 3

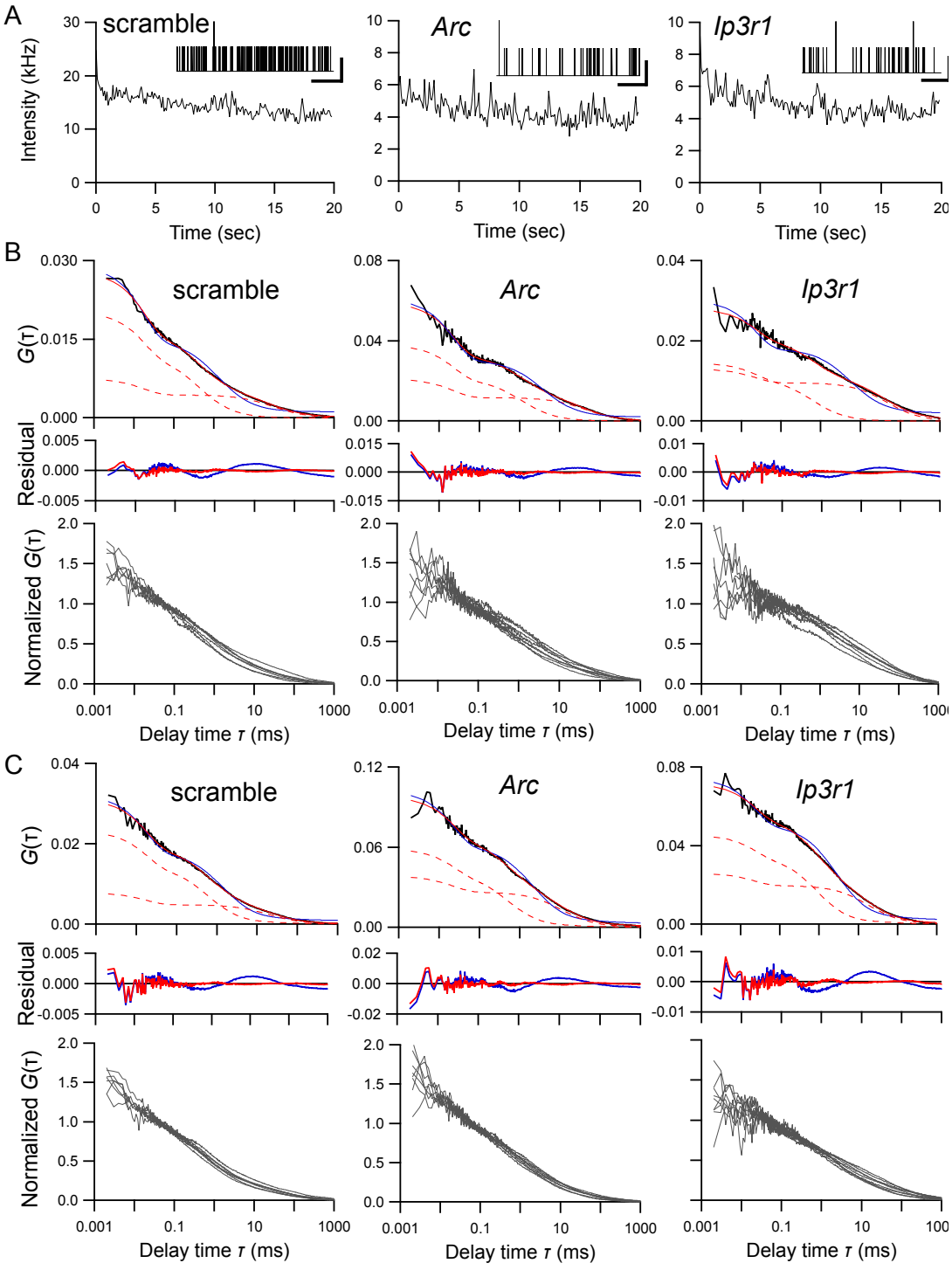
A
scramble
Arc
Ip3r1
Intensity (kHz)
Time (sec)
B
scramble
Arc
Ip3r1
G(τ)
Residual
Normalized G(τ)
Delay time τ (ms)
C
scramble
Arc
Ip3r1
G(τ)
Residual
Normalized G(τ)
Delay time τ (ms)

Figure 4

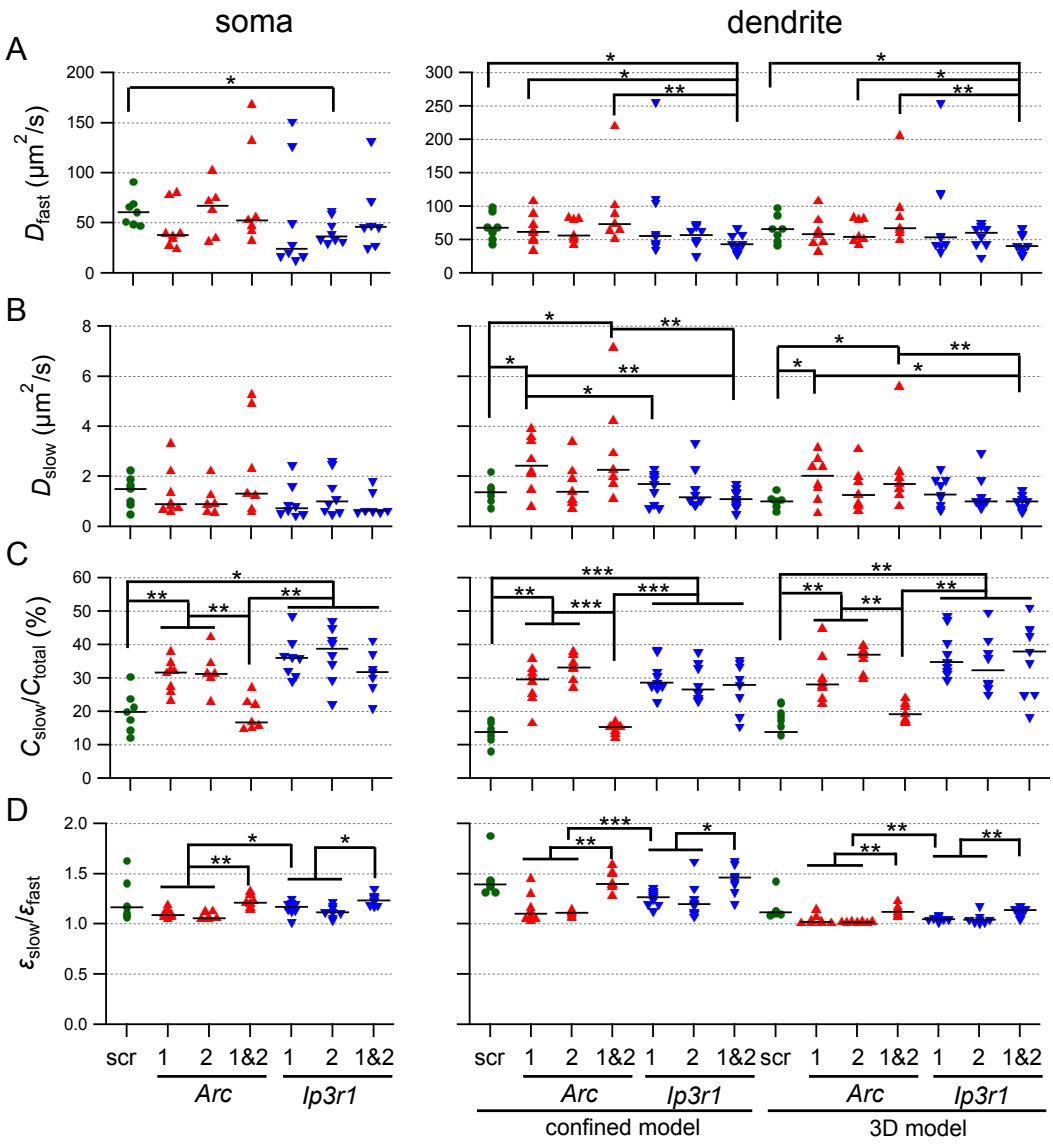
soma
dendrite
A
B
C
D
D_{fast} (µm^2/s)
D_{slow} (µm^2/s)
C_{slow}/C_{total} (%)
$\varepsilon_{slow}/\varepsilon_{fast}$
scr
1
2
1&2
Arc
Ip3r1
confined model
3D model

Figure 5

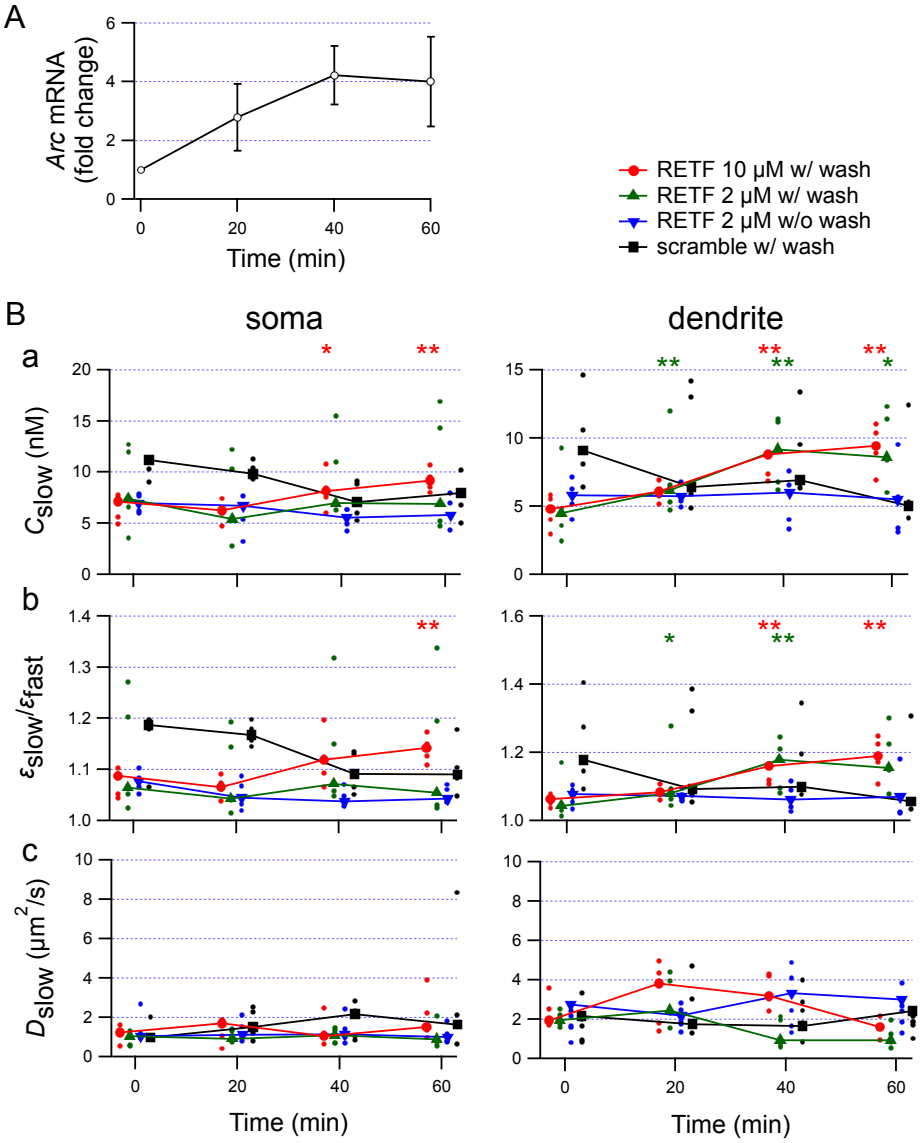
A
Arc mRNA (fold change)
Time (min)
RETF 10 μM w/ wash
RETF 2 μM w/ wash
RETF 2 μM w/o wash
scramble w/ wash
B
soma
dendrite
a
b
c
Cslow (nM)
εslow/εfast
Dslow (μm2/s)
Time (min)
Time (min)

Figure 6

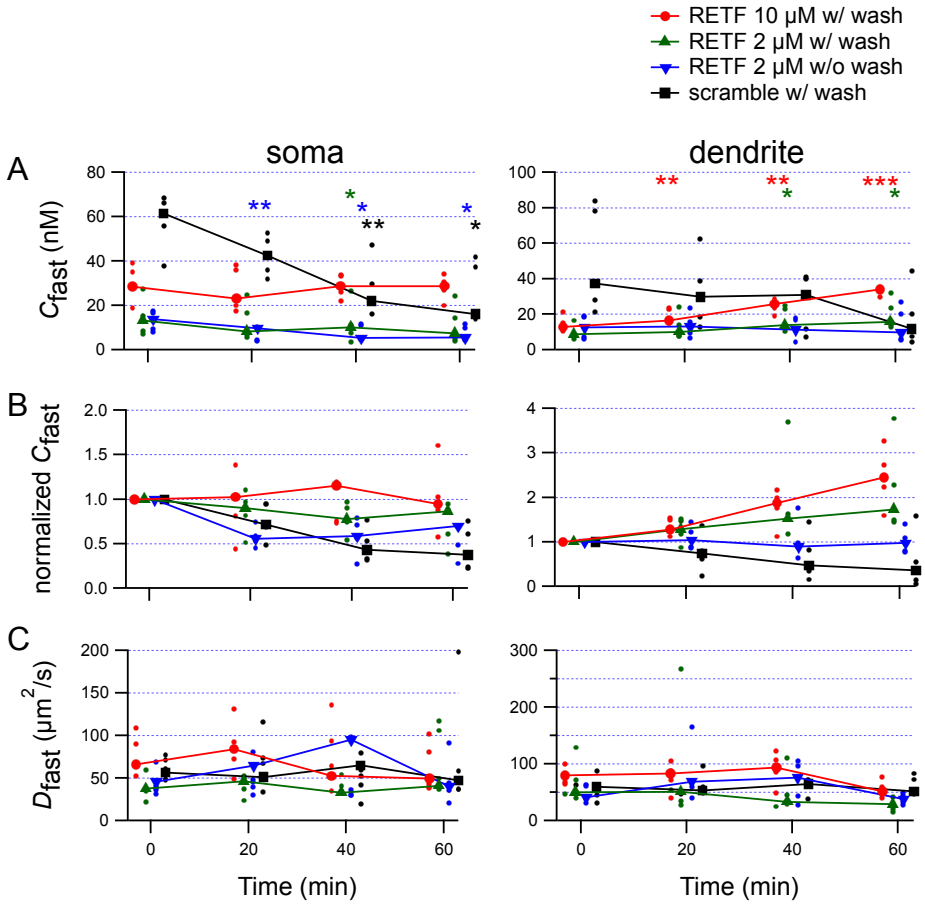
RETF 10 µM w/ wash
RETF 2 µM w/ wash
RETF 2 µM w/o wash
scramble w/ wash
soma
dendrite
A
B
C
C_{fast} (nM)
normalized C_{fast}
D_{fast} (µm^2/s)
Time (min)
Time (min)

Figure 7

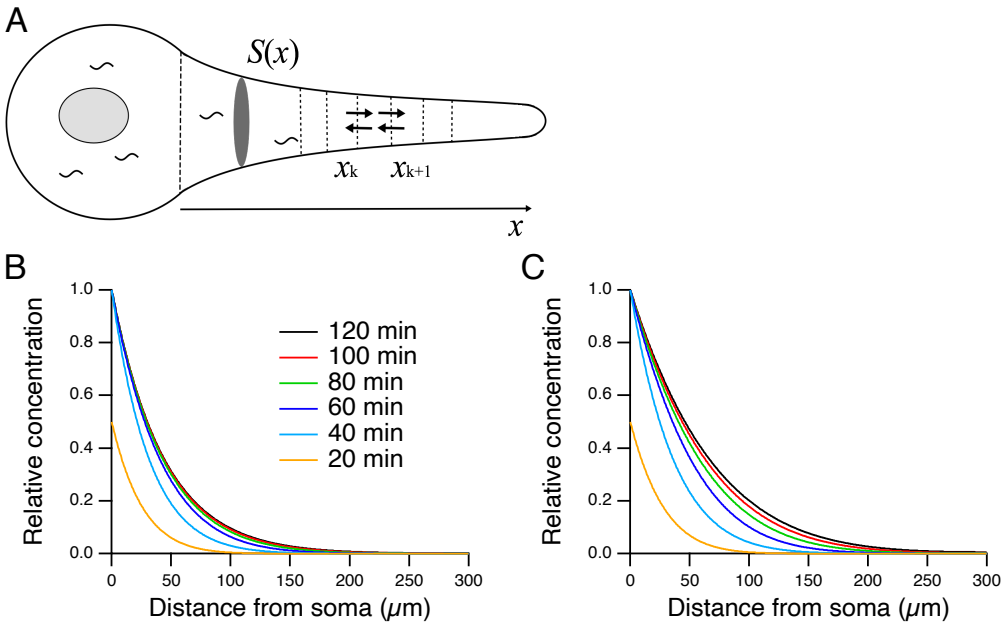
A
S(x)
x_k
x_k+1
x
B
Relative concentration
1.0
0.8
0.6
0.4
0.2
0.0
0
50
100
150
200
250
300
Distance from soma (μm)
120 min
100 min
80 min
60 min
40 min
20 min
C
Relative concentration
Distance from soma (μm)

Figure 8

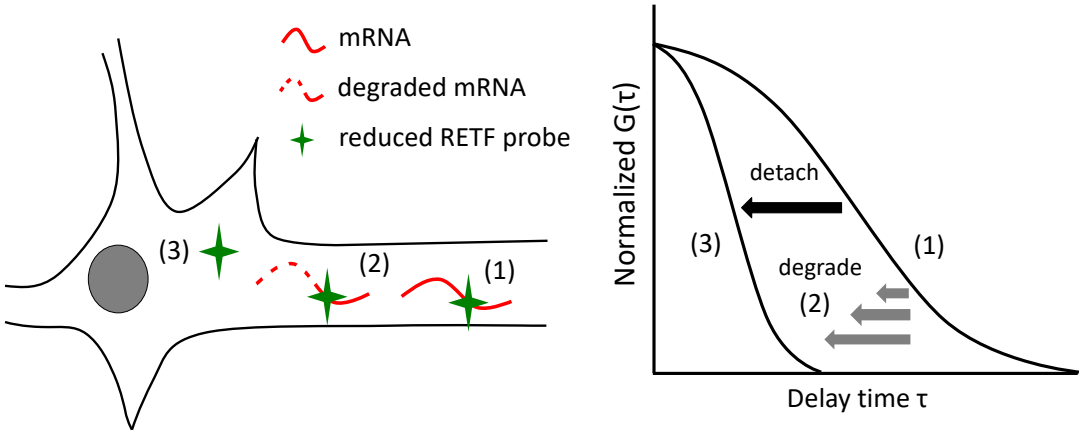
mRNA
degraded mRNA
reduced RETF probe
(3)
(2)
(1)
Normalized G(τ)
detach
(3)
(1)
degrade
(2)
Delay time τ

Figure 9

Quantification of native mRNA dynamics in living neurons using fluorescence correlation spectroscopy and reduction-triggered fluorescent probes

Hirotaka Fujita, Ryota Oikawa, Mayu Hayakawa, Fumiaki Tomoike, Yasuaki Kimura, Hiroyuki Okuno,Yoshiki Hatashita, Carolina Fiallos Oliveros, Haruhiko Bito, Toshio Ohshima, Satoshi Tsuneda, Hiroshi Abe, and Takafumi Inoue

SUPPORTING INFORMATION

Figure S1: *In vitro* FCS mesurement using *in vitro* transcribed *Arc* RNA
Figure S2: Quantification of photobleaching
Figure S3: Effect of the fluctuation in the short lag range of autocorrelation functions to fitted diffusion parameters
Figure S4: Relationship between C_{fast} and C_{slow}
Table S1: Diffusion parameters
Table S2: Diffusion parameters under stimulation

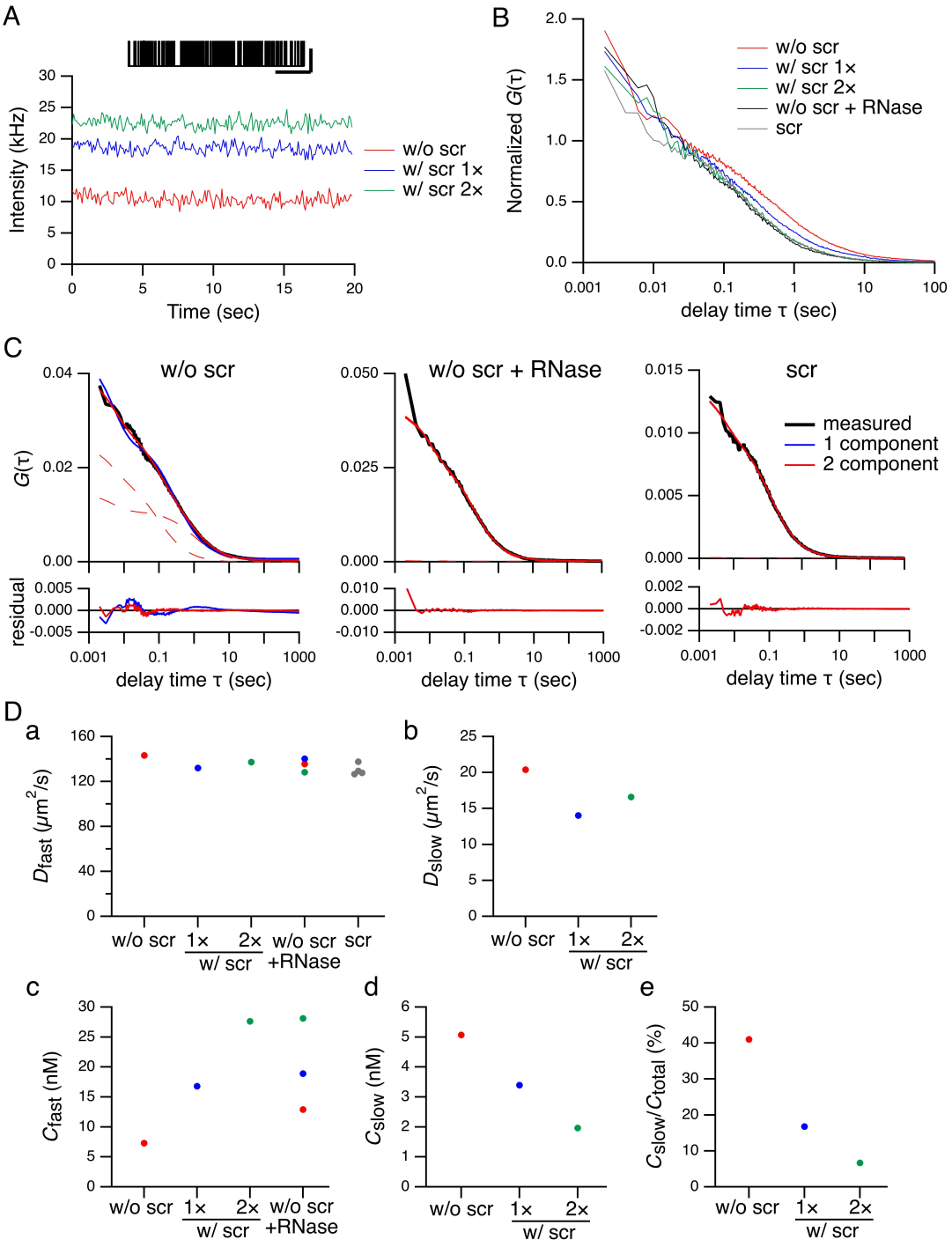

Figure S1. *In vitro* FCS measurement with *in vitro* synthesized *Arc* RNA

Aliquotes of synthetized RNA (7 µL; in the order of 30 nM) were mixed with 3 µL of 100 nM *Arc* RETF probe ("w/o scr" mixture), 3 µL of 100 nM *Arc* RETF probe and 10 µL of 30 nM scramble probe ("w/ scr 1×" mixture), or 3 µL of 100 nM *Arc* RETF probe and 20 µL of 30 nM scramble probe ("w/ scr 2×" mixture). Thus, the ratio of the final concentration of RNA in these three mixtures was 3:1.5:1; the final concentratons of RETF probe were 30, 15, and 10 nM, respectively; and the final concentrations of the scramble probe was 0, 15, and 20 nM,

respectively. Ten minutes after the mix, FCS measurements were performed. (A) Exemplifying fluorescence intensity traces after resampling at 10 Hz. Inset: representative raw photon events in the "w/o scr" mixture sampled at 1 MHz (scale bars: 2 ms and 1 MHz). (B) Normalized averaged autocorrelation functions of the "w/o scr", "w/ scr 1×", and "w/ scr 2×" mixtures (7, 7, and 6 measurements, respectively). After FCS mesurement, 1, 2, and 3 μL RNase solutions were added to the "w/o scr", "w/ scr 1×", and "w/ scr 2×" mixtures, respectively, and FCS measurements were performed 10 min later; only the "w/o scr + RNase" result is shown (8, 8, and 10 measurements, respectively). FCS mesurements with only the scramble probe ("scr only" mixture; 50 nM; 9 measurements) were also performed. (C) Averaged autocorrelation functions of the "w/o scr" mixture (left), the "w/o scr" mixture after addition of RNase (middle), and the "scr only" (right) mixture are fitted to one- and two-component 3D diffusion models. Dashed red lines represent each component of the two-component fit results. While the autocorrelation function of the "scr only" and "w/o scr + RNase" mixtures were fitted well to the one-component diffusion model, that of the "w/o scr" mixture consisted of a slowly diffusing component in addition to a faster diffusing component. (D) Diffusion coefficients of the faster (a; D_{fast}) and slower (b; D_{slow}) components, concentration of the faster (c; C_{fast}) and slower (d; C_{slow}) components and the ratio of C_{slow} to that of the total concentration (e; C_{slow}/C_{total}) of the "w/o scr" (red), "w/ scr 1×" (blue), "w/ scr 2×" (green), and "scr only" (gray) mixtures together with the results of the "w/o scr", "w/scr 1×", and "w/ scr 2×" mixutures after addition of RNase ("+RNase") with the same colors to those before RNase addition. Since the amounts of slower components of the "+RNase" and "scr only" mixtures were very small ($C_{slow}/C_{total} < 1\%$), the one-component diffusion model was thought to be more appropreate than the two-component fit for these data set. Threfore, D and C of one-component fitting of the "+RNase" and "scr only" mixtures are used instead of D_{fast} and C_{fast}. Although Kd between RNA and RETF probe could be deduced from the C_{slow} value together with the concentrations of RNA and RETF probe on the assumption that the C_{slow} value reflects the concentration of RNA-RETF probe complex, we do not describe about the Kd value here because of the uncertainity of the synthetized RNA concentraton. In the absense of template RNA, the *Arc* RETF probe did not show detectable fluorescence signal and thereby reasonable autocorrelation curves (data not shown).

Methods: The mouse *Arc* open reading frame (ORF) and a DNA fragment containing the 5' UTR of the *Arc* gene were separately amplified by PCR using C57BL/6 mouse genomic DNA as a template. The 3' UTR of the *Arc* gene was amplified by RT-PCR using total RNA extracted from the cerebral cortex of C57BL/6 mice. The 5' UTR, ORF, and 3' UTR fragments of the mouse *Arc* gene were assembled and subcloned into the EcoRI and XhoI sites of the pcDNA3 vector. The resultant plasmid was designated as pcDNA3-mus-Arc-UTRs. The entire sequences of the *Arc* ORF with 5' and 3' UTRs were confirmed by sequencing. pcDNA3-mus-Arc-UTRs was linealized with XhoI and used as a template, from which 3.0 kb-length RNA is transcribed. After RNA synthesis using mMessage mMachine Kit (Invitrogen Japan), the template DNA was digested with TURBO DNase (Invitrogen Japan), and produced RNA was confirmed with gel electrophoresis. Aliquotes of RNA (in the order of 30 nM as final concentration; estimated by the electrophoresis intensity) were incubated for 10 min with the *Arc* target 1 RETF probe, of which target sequence was completely conserved between rat and mouse *Arc* mRNA, with or without the scramble probe. Each FCS measurement was performed for 20 s with pinhole apperture 150 μm. RNaseA (1 μg/μl as final concentration; nacalai tesque, Kyoto, Japan) was used as described above.

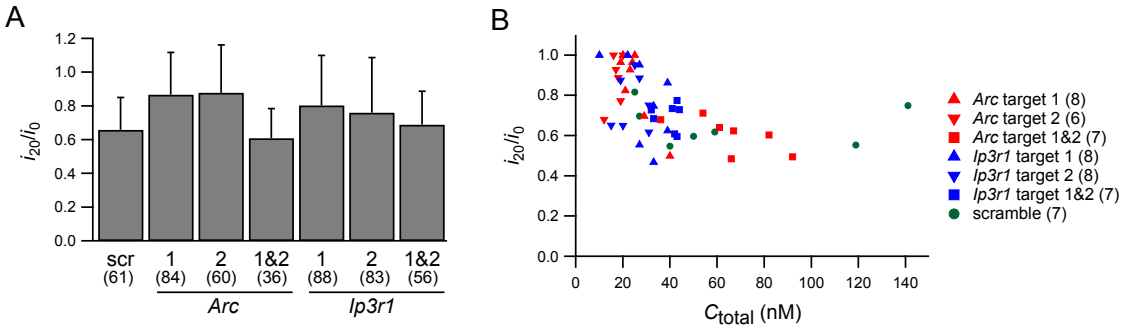

Figure S2. Quantification of photobleaching

(A) Level of photobleaching of the probe sets. Fluorescence traces measured in somata for 20 s were fitted to a double exponential function, $i(t) = i_0 + i_1 \cdot \exp(t/t_{B1}) + i_2 \cdot \exp(t/t_{B2})$. The photobleaching parameter, i_{20}/i_0, was calculated using the fit results. The number of recordings (20 s) is indicated below in parentheses. Means and s.d. are indicated. **(B)** Relationship between the photobleaching parameter averaged for each cell and the total concentration of fluorescent probes, which was obtained by FCS analysis (Fig. 5). A positive relationship between the photobleaching magnitude and probe concentration can be read from the plot. The number of cells is indicated in parentheses in the legend.

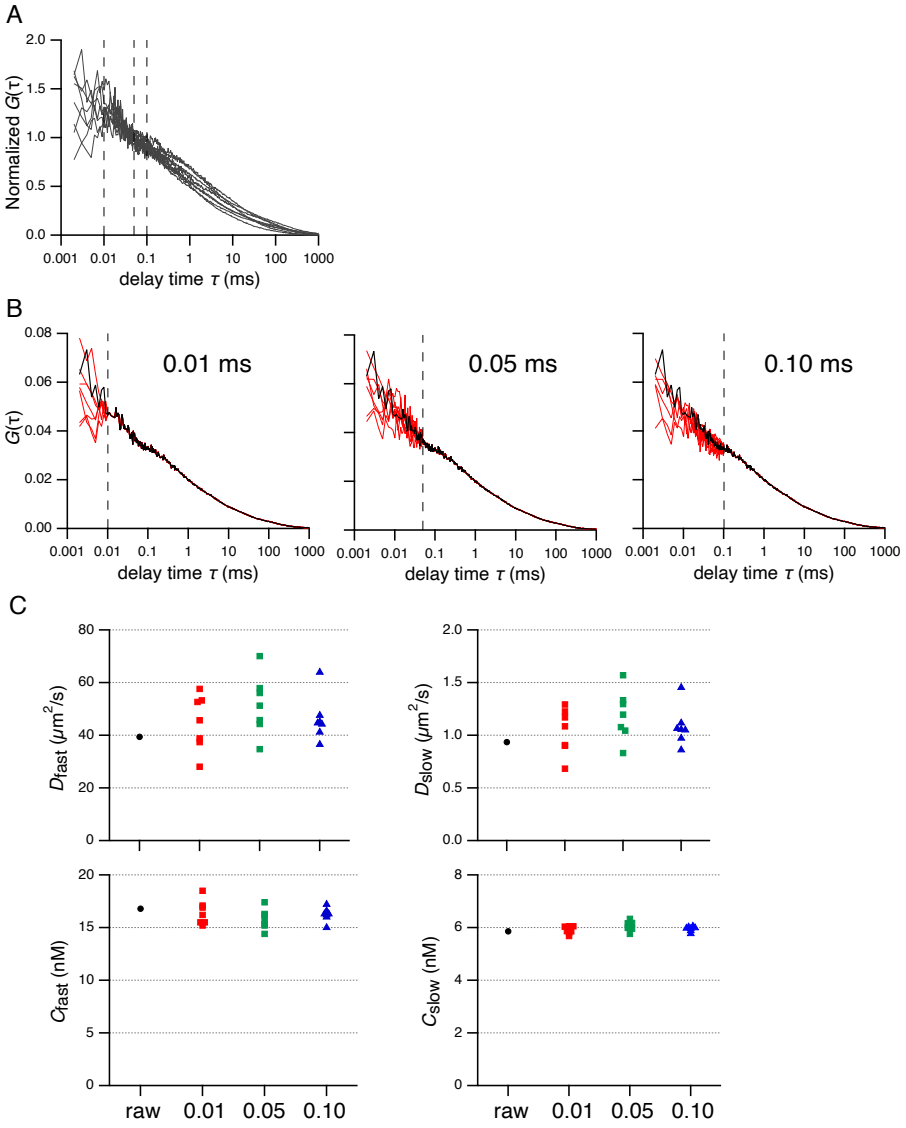

Figure S3. Effect of the fluctuation in the short lag range of autocorrelation functions to fitted diffusion parameters

(A) Autocorrelation functions taken at neuron somata with the target 1 *Arc* RETF probe: autocorrelation functions are averaged for each cell and superposed after normalization by the G(0) values (same as Fig. 4B, left bottom). (B) The fast part of autocorrelation function of a particular cell chosen randomly from the cells in A ($G_k(\tau)$; black line) was swapped with the same range of other cells ($G_i(\tau)$; red lines) after scaling to synthesize chimeric autocorrelation functions $G_i'(\tau)$:

$$G_i'(\tau) = \begin{cases} G_i(\tau) \times \frac{G_k(\tau')}{G_i(\tau')} & (\tau < \tau') \\ G_k(\tau) & (\tau \geq \tau') \end{cases}$$

(C) FCS parameters deduced by fitting the two-component 3D diffusion model with triplet-state correction to the synthetic autocorrelation functions in B. The original fitting result of $G_k(\tau)$ (raw; black marker) was changed by the swapping of the fastest ranges at the lag points (τ' ; 0.01, 0.05 and 0.1 ms; dashed lines in A–B).

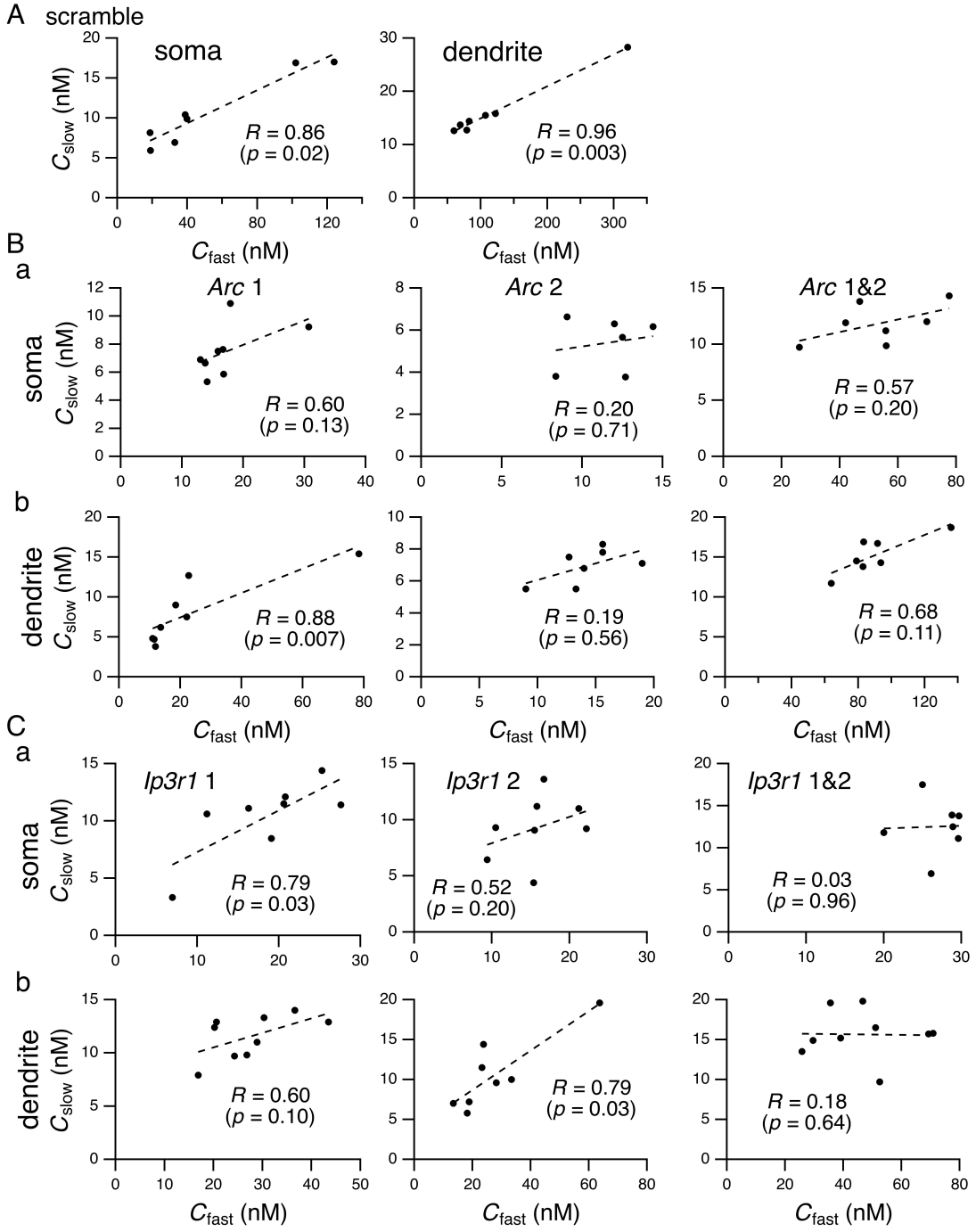

Figure S4. Relationship between C_{fast} and C_{slow}

Scatter plots of C_{slow} and C_{total} of the scramble probe **(A)**, the *Arc* **(B)** and the *Ip3r1* RETF probes **(C)** in the soma (left of A, Ba, Ca) and dendrite (right of A, Bb, Cb), which were deduced from the results shown in Fig. 5. Each dot represents the result of single neurons. Correlation coefficients (R) and p-values between C_{slow} and C_{total} assessed with Spearman test are indicated.

Table S1. Diffusion parameters

Probe		[1]loc	[2]n	[3]model	D_{fast} (μm²/s)	D_{slow} (μm²/s)	C_{slow}/C_{total} (%)	C_{fast} (nM)	C_{slow} (nM)	$\varepsilon_{slow}/\varepsilon_{fast}$ (a.u.)
scramble		S	7	3D	61 (50–67)	1.5 (0.93–1.8)	20 (16–22)	39 (26–71)	9.9 (7.5–14)	1.17 (1.10–1.29)
		D	7	conf	67 (55–80)	1.4 (1.1–1.5)	14 (12–16)	83 (74–1.1×10²)	14 (13–16)	1.39 (1.34–1.43)
				3D	66 (52–76)	1.0 (0.86–1.1)	19 (16–21)	33 (30–47)	8.1 (7.6–9.1)	1.12 (1.10–1.13)
Arc	target 1	S	8	3D	38 (33–49)	0.89 (0.72–1.6)	32 (27–33)	16 (14–17)	7.2 (6.5–8.0)	1.09 (1.07–1.11)
		D	8	conf	62 (50–77)	2.4 (2.0–3.4)	30 (25–32)	16 (12–22)	6.9 (4.8–9.9)	1.10 (1.05–1.20)
				3D	59 (46–67)	2.0 (1.4–2.5)	28 (26–31)	6.8 (5.2–8.6)	3.0 (2.0–4.9)	1.02 (1.01–1.04)
	target 2	S	6	3D	67 (42–74)	0.89 (0.64–1.2)	31 (30–34)	12 (10–13)	5.9 (4.3–6.3)	1.06 (1.05–1.11)
		D	7	conf	56 (51–81)	1.4 (1.0–2.1)	33 (31–36)	14 (13–16)	7.1 (6.1–7.6)	1.11 (1.08–1.12)
				3D	54 (50–81)	1.3 (0.86–1.9)	37 (33–39)	5.8 (5.5–6.4)	3.4 (2.9–3.6)	1.02 (1.01–1.02)
	target 1&2	S	7	3D	52 (45–94)	1.3 (0.96–3.6)	17 (15–22)	56 (44–63)	12 (11–13)	1.21 (1.18–1.26)
		D	7	conf	73 (64–95)	2.3 (1.8–3.6)	15 (14–15)	83 (81–93)	15 (14–17)	1.40 (1.38–1.51)
				3D	67 (63–91)	1.7 (1.4–2.1)	19 (17–22)	35 (32–37)	8.5 (7.3–10)	1.12 (1.09–1.16)
Ip3r1	target 1	S	8	3D	24 (17–69)	0.74 (0.53–1.1)	36 (32–38)	20 (15–22)	11 (10–12)	1.17 (1.14–1.21)
		D	9	conf	56 (43–1.1×10²)	1.7 (0.87–2.0)	29 (28–32)	27 (21–30)	12 (9.8–13)	1.27 (1.20–1.31)
				3D	54 (43-1.2×10²)	1.3 (0.85–1.9)	35 (32–40)	11 (7.3–12)	6.5 (5.0–7.1)	1.05 (1.04–1.06)
	target 2	S	8	3D	37 (34–51)	1.0 (0.63–1.8)	39 (33–42)	16 (14–18)	9.3 (8.4–11)	1.12 (1.10–1.17)
		D	8	conf	57 (47–65)	1.2 (1.0–1.7)	27 (24–33)	24 (19–30)	9.8 (7.2–12)	1.20 (1.11–1.27)
				3D	61 (44–67)	1.0 (0.89–1.3)	32 (28–38)	8.5 (8.0–12)	4.8 (3.2–6.6)	1.04 (1.02–1.05)
	target 1&2	S	7	3D	46 (37–60)	0.63 (0.60–1.0)	32 (29–35)	29 (26–29)	13 (12–14)	1.23 (1.19–1.27)
		D	9	conf	43 (34–56)	1.1 (0.86–1.4)	28 (18–33)	47 (36–53)	16 (15–17)	1.46 (1.40–1.48)
				3D	40 (32–57)	1.0 (0.72–1.1)	38 (25–44)	15 (11–22)	9.0 (8.0–9.8)	1.14 (1.10–1.15)

Result in Fig. 5 are shown numerically with the first and third quartiles.

[1]loc: location, S (soma) or D (dendrite)

[2]n: number of cells

[3]model: diffusion model, 3D (3D diffusion model) or conf (confined diffusion model)

Table S2. Diffusion parameters under stimulation

probe		[1]loc	[2]n	[3]time	C_{slow} (nM)	D_{slow} (μm^2/s)	$\varepsilon_{slow}/\varepsilon_{fast}$ (a.u.)	C_{fast} (nM)	D_{fast} (μm^2/s)
scramble		S	5	0	11 (10–11)	0.98 (0.97–1.0)	1.19 (1.18–1.20)	61 (56–66)	62 (49–67)
				20	9.8 (9.5–10)	1.5 (1.2–2.3)	1.17 (1.16–1.18)	42 (36–49)	67 (53–72)
				40	7.1 (6.0–8.9)	2.2 (1.0–2.3)	1.09 (1.07–1.13)	22 (22–30)	60 (53–80)
				60	8.0 (6.8–8.0)	1.6 (1.6–2.1)	1.09 (1.08–1.10)	16 (15–37)	50 (39–58)
		D	5	0	9.1 (8.1–11)	2.2 (1.6–2.2)	1.18 (1.15–1.27)	38 (28–78)	60 (45–62)
				20	6.4 (5.9–13)	1.7 (1.4–2.5)	1.09 (1.08–1.32)	30 (19–39)	53 (49–59)
				40	6.9 (6.6–9.5)	1.7 (1.3–4.1)	1.10 (1.10–1.20)	31 (12–40)	65 (38–69)
				60	5.1 (4.8–5.3)	2.4 (1.3–2.7)	1.06 (1.05–1.06)	12 (7.5–20)	51 (47–72)
RETF Arc target2	10 μM	S	5	0	7.1 (5.6–7.5)	1.2 (1.2–1.3)	1.09 (1.05–1.09)	29 (28–35)	66 (52–90)
				20	6.3 (6.0–6.4)	1.7 (1.1–1.9)	1.07 (1.06–1.07)	23 (20–36)	84 (50–92)
				40	8.2 (7.6–8.4)	1.0 (1.0–1.2)	1.12 (1.09–1.12)	29 (26–33)	53 (41–65)
				60	9.2 (8.6–9.5)	1.5 (1.4–2.2)	1.14 (1.13–1.15)	29 (27–31)	50 (43–80)
		D	5	0	4.8 (4.0–5.5)	1.9 (1.9–2.5)	1.06 (1.05–1.07)	13 (12–15)	80 (68–82)
				20	6.1 (5.8–6.2)	3.8 (1.8–4.4)	1.08 (1.08–1.09)	17 (16–23)	83 (71–88)
				40	8.8 (7.4–8.8)	3.2 (3.0–4.2)	1.16 (1.12–1.17)	26 (24–26)	94 (86–1.1×10^2)
				60	9.4 (8.9–10)	1.6 (1.5–1.6)	1.19 (1.17–1.23)	34 (34–35)	52 (50–60)
	2 μM	S	5	0	7.4 (6.6–12)	1.0 (0.61–1.1)	1.06 (1.05–1.20)	13 (8.5–15)	38 (35–59)
				20	5.4 (5.4–10)	0.91 (0.79–1.3)	1.04 (1.04–1.14)	8.2 (6.7–17)	46 (37–52)
				40	7.0 (6.8–11)	1.1 (0.71–1.4)	1.07 (1.06–1.15)	10 (7.7–11)	33 (32–34)
				60	6.9 (5.2–14)	0.89 (0.73–0.92)	1.06 (1.03–1.20)	7.3 (5.0–15)	41 (37–1.1×10^2)
		D	5	0	4.5 (3.6–4.8)	2.0 (1.7–2.2)	1.04 (1.03–1.05)	8.7 (8.5–9.1)	50 (47–71)
				20	6.2 (5.4–6.6)	2.4 (2.3–3.9)	1.08 (1.06–1.09)	10 (8.1–14)	51 (35–54)
				40	9.2 (6.8–11)	0.92 (0.69–2.0)	1.18 (1.10–1.21)	14 (14–23)	33 (29–46)
				60	8.6 (8.4–11)	0.93 (0.85–1.3)	1.16 (1.15–1.23)	16 (14–24)	29 (20–41)
	2 μM [4]no stim	S	5	0	7.0 (6.2–7.7)	1.1 (0.96–1.2)	1.08 (1.07–1.08)	14 (9.3–17)	38 (36–40)
				20	6.7 (5.4–6.8)	1.1 (0.98–1.6)	1.05 (1.03–1.07)	9.8 (4.3–9.8)	45 (40–48)
				40	5.6 (5.0–6.4)	1.1 (0.97–1.4)	1.04 (1.04–1.05)	5.3 (4.8–11)	33 (30–37)
				60	5.8 (5.8–7.0)	1.0 (0.79–1.2)	1.04 (1.04–1.06)	5.7 (4.9–9.7)	41 (35–44)
		D	5	0	5.8 (5.1–6.2)	1.7 (0.94–2.0)	1.08 (1.05–1.09)	13 (7.2–18)	41 (38–61)
				20	5.7 (5.4–6.7)	1.8 (1.8–3.0)	1.07 (1.06–1.08)	13 (9.2–16)	69 (59–70)
				40	6.0 (4.0–6.5)	2.4 (1.8–2.9)	1.06 (1.04–1.09)	11 (11–17)	76 (43–96)
				60	5.5 (3.4–5.7)	1.9 (1.7–1.9)	1.07 (1.03–1.07)	9.8 (6.2–20)	38 (32–44)

Results indicated in Figs. 6 and 7 are shown numerically. Medians with the first and third quartiles are indicated. Just after 0 min

[1]loc: location, S (soma) or D (dendrite)

[2]n: number of cells

[3]time: time after stimulation (TTX washout, min)

[4]no stim: TTX was not washed